Colloquium: Nonlinear energy localization and its manipulation in micromechanical oscillator arrays

M. Sato, B. E. Hubbard, and A. J. Sievers

Laboratory of Atomic and Solid State Physics, Cornell University, Ithaca, New York 14850-2501, USA

(Published 26 January 2006)

It has been known for some time that nonlinearity and discreteness play important roles in many branches of condensed-matter physics as evidenced by the appearance of domain walls, kinks, and solitons. A recent discovery is that localized dynamical energy in a perfect nonlinear lattice can be stabilized by the lattice discreteness. Intrinsic localized modes (ILMs) are the resulting signature. Their energy profiles resemble those of localized modes at defects in a harmonic lattice but, like solitons, they can move. ILMs have been observed in macroscopic arrays as diverse as coupled Josephson junctions, optical waveguides, two-dimensional nonlinear photonic crystals, and micromechanical cantilevers. Such dynamically driven localized modes are providing a new window into the underlying simplicity of nonequilibrium dynamics. This Colloquium surveys the studies of ILMs in micromechanical cantilever arrays. Because of the ease of sample fabrication with silicon technology and the intuitive optical visualization techniques, these experiments are able to demonstrate the general nature and properties of dynamical energy localization while at the same time providing new information on ILM generation, locking, pinning, and interaction with impurities.

DOI: 10.1103/RevModPhys.78.137 PACS number(s): 63.20.Pw, 42.65.Sf, 85.85.+j

CONTENTS

I. INTRODUCTION

A. Historical background

The study of wave propagation in discrete lattices has a rich history that goes back to Newton (Brillouin, 1946). The first demonstration of its importance in condensed-matter physics was put forward by Debye (1912) with zones introduced somewhat later by Brillouin and others (Brillouin, 1946). Then in the 1940s Lifshitz and collaborators (Maradudin *et al.*, 1971) demonstrated that even the dynamics of defects in discrete harmonic lattices could be quantified in this way and showed that localized vibrational modes at defect sites were a new feature. Such defect-induced localized modes have been studied both theoretically and experimentally in great detail (Maradudin, 1969; Newman, 1969; Sievers, 1969; Maradudin *et al.*, 1971; Barker and Sievers, 1975; Bilz *et al.*, 1984). This includes studies of small mass and large force constant defects in monatomic lattices where a localized vibrational mode may appear above the plane-wave acoustic spectrum as well as for diatomic and more

complex lattices where localized modes can be found at frequencies in the gap between the acoustic and optic branches or above the optic branch. (When the lattice cells vibrate in phase in the long-wavelength limit this motion is associated with an acoustic branch and when they vibrate out of phase it is called an optic branch.) If a large mass or weak force constant defect occurs then localized resonant modes and tunneling states can appear in the acoustic spectrum (Greene and Sievers, 1982). Finally if the size of the defect space is still larger then a variety of localized vibrational modes may occur, including pocket modes, where the large vibrational amplitude appears on defect neighbor sites rather than on the defect itself (Sandusky *et al.*, 1991; Grant *et al.*, 1998).

For nonlinear periodic discrete structures, the time scale of discovery has been significantly shorter. The first numerical study of the nonlinear dynamics of a one-dimensional (1D) crystal lattice by Fermi, Pasta, and Ulam (1955) in the 1950s produced surprising recurring dynamical results, which subsequently motivated the discovery of the 1D soliton for continuum systems (Zabusky and Kruskal, 1965; Remoissenet, 1999). These localized traveling waves maintain their shape as they move and, in addition, when two of them meet they pass through each other with only a phase change. For a monatomic lattice such solitons (called "lattice solitons") were identified in 1981 for a special two-body potential that permits integration of the equations of motion (Toda, 1989). Note that for a di-element Toda lattice a localized traveling wave no longer passes through another unscathed, i.e., the equations of motion are not integrable (Kevrekidis and Malomed, 2002). Such nonsolitonlike behavior of a localized traveling wave in a Fermi-Pasta-Ulam lattice kept researchers focused on the 1D integrable soliton systems until the late 1980s when it was shown that the localization of energy produced by nonlinearity in a discrete lattice with an excitation in the frequency gap extending only over a few lattice sites resembled that produced by a linear force constant defect in a harmonic lattice (Dolgov, 1986; Sievers and Takeno, 1988). Like a soliton, such localized energy can propagate; however, in contrast to a soliton, collisions between such excitations result in energy transfer between them with the more localized excitation stealing energy from the less localized ones (Burlakov and Kiselev, 1991; Dauxois and Peyrard, 1993; Kiselev *et al.*, 1995; Sievers and Page, 1995; Flach and Willis, 1998; Lai and Sievers, 1999; Campbell *et al.*, 2004). Another difference is that these localized excitations can occur in a lattice of any dimension (Kiselev and Sievers, 1997). To distinguish these excitations from defect localized modes they are called intrinsic localized modes (ILMs) (Sievers and Takeno, 1988). To contrast their properties with solitons in continuous media they are often referred to as "discrete breathers" (Flach and Willis, 1998; Flach, 2004) or lattice solitons (Christoldoulides and Joseph, 1988; Fleischer, Carmon, *et al.*, 2003; Fleischer, Segev, *et al.*, 2003). Note that this definition of a lattice soliton is different from the one mentioned above (Toda, 1989).

What is required to produce ILMs? If the frequencies of the plane-wave modes increase with increasing amplitude then the lattice potential is referred to as "hard," while if the converse occurs then the lattice potential is "soft" (Marion, 1970). For a frequency gapped plane-wave spectrum of acoustic and optic modes some modes become unstable at large amplitude. If the curvature of the dispersion curve in the region of a bounding mode has negative curvature and the lattice potential is hard then at large amplitude this plane-wave mode becomes unstable with respect to formation of an ILM in the gap above the plane-wave spectrum. An important dimensionless parameter, which defines a large amplitude, is the nonlinear potential term times the amplitude to the appropriate power divided by the harmonic potential term. When this parameter is $\geqslant 0.5$, ILMs tend to form. For a soft lattice potential and positive curvature of the dispersion curve the ILM drops from the optic branch into the frequency gap. Since it is the lattice nonlinearity together with the vibrational amplitude that determine when ILMs can appear, even a lattice with a small nonlinearity when strongly driven may produce ILMs.

Initial theoretical studies with toy lattices have now progressed to the systematic examination of more realistic lattice models. These cover the areas of nonlinear crystal dynamics (Page, 1990; Kiselev *et al.*, 1993; Bickham *et al.*, 1997; Kiselev and Sievers, 1997; Rössler and Page, 1997, 2000), magnetic lattices (Wallis *et al.*, 1995; Rakhmanova and Mills, 1996; Lai and Sievers, 1999), electron-phonon systems (Wang *et al.*, 1998; Fehske *et al.*, 2000), tailored optical materials (Bang and Miller, 1996; Eisenberg *et al.*, 1998; McGurn, 2002), and lattice-assisted energy and charge transfer in polarizable matter (Fehske *et al.*, 2001).

Since the theoretical predictions for ILMs apply quite generally to lattices in any dimension that exhibit both nonlinearity and discreteness, such localized energy "hot spots" may appear on different length scales in many scientific fields. In recent years a few experiments have been carried out on atomic lattices. They are (i) charge transfer solid PtCl (Swanson *et al.*, 1999; Fehske *et al.*, 2001), where analysis of resonance Raman spectra was used to identify localized vibrational modes; (ii) quasi-1D antiferromagnetic chains, where a high power microwave source was used to produce ILMs out of equilibrium (Schwarz *et al.*, 1999; English *et al.*, 2001; Sato *et al.*, 2002) and where steady-state locking of ILMs has recently been achieved (Sato and Sievers, 2004); (iii) bcc ^{4}He (Markovich *et al.*, 2002), where inelastic neutron scattering shows an anomalous opticlike mode for this monatomic crystal; (iv) proteins (Xie *et al.*, 2000; Austin *et al.*, 2003), where picosecond pump probe measurements of the amide I band indicate a self-trapped vibrational state; and (v) hydrogen-bonded acetanilide (Edler and Hamm, 2004), where spectral anomalies are interpreted as a signature of vibrational self-trapping. In all five kinds of studies direct observation of energy localization has not been possible and observed transitions,

spectroscopic frequency shifts, or relaxation times of spectral elements are connected to localization by theoretical and numerical analysis.

Although such indirect spectroscopic experiments may be the key to addressing major unsettled questions regarding the behavior of nonclassical energy localization in discrete lattices, in order to better understand and visualize the general experimental properties of such nonlinear excitations, different macroscopic lattice experiments have been developed (Chen, 1994; Lou and Huang, 1995; Marquie *et al.*, 1995; Binder *et al.*, 2000; Trías *et al.*, 2000; Fleischer, Carmon, *et al.*, 2003; Mandelik *et al.*, 2003; Sato, Hubbard, Sievers, *et al.*, 2003). Particularly enlightening have been those experimental studies that use laser observational methods. These range from the technique of low-temperature laser scanning spectroscopy, to observe localized excitations in Josephson-junction arrays (Ustinov, 2003), to the identification of discrete solitons in optically induced real time waveguide arrays (Fleischer, Segev, *et al.*, 2003), to the optical imaging and manipulation of localized vibrational modes in cantilever arrays, the topic of this Colloquium (Sato, Hubbard, English, *et al.*, 2003; Sato *et al.*, 2004).

B. Micromechanical array model

The nonlinear localization phenomenon of interest can be illustrated with a simple mass and spring lattice, which, as demonstrated later, can also be used to describe the nonlinear dynamics of micromechanical arrays. Figure 1(a) shows a 1D mass and spring lattice. This generic model identifies linear and nonlinear restoring force coefficients due to both onsite and intersite coupling between particles. It is mono-element when $A=B$ and di-element when $A\neq B$. The equation of motion for each mass is

$$m_i\frac{d^2x_i}{dt^2}+k_{2Oi}x_i+k_{4Oi}x_i^3+k_{2I}(2x_i-x_{i-1}-x_{i+1}) + k_{4I}[(x_i-x_{i-1})^3+(x_i-x_{i+1})^3]=0, \quad (1)$$

where i (even) identifies site A and i (odd), site B, k_{2Oi} and k_{4Oi} are the coefficients of the onsite harmonic and hard quartic potential terms, while k_{2I} and k_{4I} identify the corresponding intersite terms. For the mono-element *harmonic* lattice the resulting linear dispersion curve for the plane-wave solutions has a gap below the acousticlike branch illustrated by the solid curve in Fig. 1(b) while the corresponding dispersion curve for the di-element lattice (dashed curves) has the additional frequency gap between the acoustic and optic branches.

The combination of discreteness and nonlinearity ensures that, in addition to the usual extended-wave excitations, intrinsic localized excitations may occur anywhere in the perfect periodic lattice given sufficient vibrational amplitude. For the case of hard anharmonicity ($k_4>0$) in the mono-element lattice two such localized eigenvectors are shown in Fig. 1(b). In these cases, for illustration purposes, the hard quartic nonlinearity in the potential is chosen to have a fixed value but to be placed at either the intersite location or the onsite one to make a particular point about localization. A nonlinear minimization scheme is used to find the localized eigenvectors and the amplitudes of the excitations are then varied until the resulting ILMs have the same vibrational energy. The local mode at $\omega/\omega_0=2.89$ occurs for a lattice with only hard quartic *intersite* nonlinearity while the local mode at $\omega/\omega_0=2.26$ is for a lattice with only hard quartic *onsite* nonlinearity. The ratio of the maximum amplitude of the former to the latter is 1.55. These two examples demonstrate (i) that localization can occur when the nonlinearity is onsite or intersite and (ii) for a given dynamical energy the resulting localization is strongest for the intersite case. For micromechanical cantilever arrays the intersite nonlinearity will turn out to provide the dominant contribution that produces dynamical energy localization.

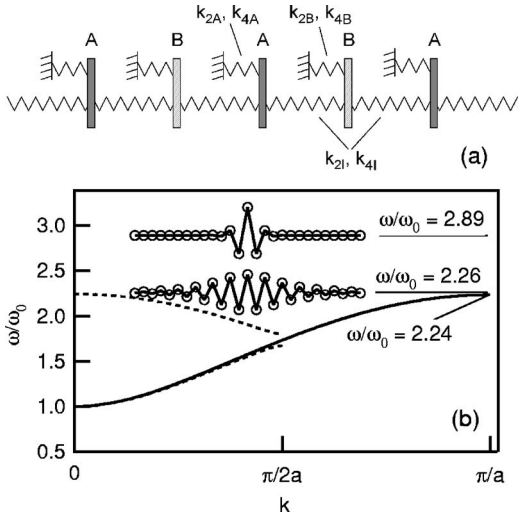

FIG. 1. Mass-and-spring nonlinear lattice model. (a) A and B represent two different masses per unit cell, each with nearest-neighbor intersite and onsite restoring force springs. Both types of springs possess a harmonic and hard quartic potential energy. (b) Dispersion curve (solid) for a mono-element lattice for the harmonic limit with dimensionless parameters $m=1$, $k_{2O}=1$, $k_{2I}=1$ in Eq. (1). The frequency gap below the $k=0$ mode is produced by the onsite energy term. Dotted curves: Linear dispersion relation for a di-element harmonic lattice with parameters $m_A=1.1$, $k_{2A}=1.1$, $m_B=0.9$, $k_{2B}=0.9$. Superimposed on the graph are two examples showing the real space shapes of nonlinear ILM eigenfunctions. These functions were calculated for the mono-element lattice such that they have the same dynamical energy and the same nonlinearity placed at one of two possible lattice locations. With only onsite nonlinearity a broad eigenmode appears at $\omega/\omega_0=2.26$, while with only intersite nonlinearity a sharp eigenmode mode appears at $\omega/\omega_0=2.89$.

C. Overview and organization

The experiments on silicon-nitride cantilever arrays have been quite successful in providing data on a number of theoretically predicted ILM properties, such as

their interaction with an ac driver (Rössler and Page, 1995, 2000; Lai and Sievers, 1999), their propagation (Bickham *et al.*, 1992; Sandusky *et al.*, 1992; Flach and Willis, 1994), directed transport (Zheng *et al.*, 2002), and amplitude dependent mobility in a discrete lattice potential (Bickham *et al.*, 1993; Flach and Willis, 1994; Bang and Peyrard, 1995), as well as their interactions with impurities (Bourbonnais and Maynard, 1990, 1992; Kivshar, 1991; Kiselev *et al.*, 1994). These findings are of fundamental interest for revealing the underlying general nature of intrinsic localization and are of applied interest for the design of coupled micro-electro-mechanical system (MEMS) and nano-electro-mechanical system (NEMS) structures. An important application relevant to the study of nonlinear dynamics of periodic arrays stems from the development of silicon micromechanics leading to the generation of microinstruments for high-precision measurements, where often the dynamics show nonlinear behavior (Evoy *et al.*, 1999; Chan *et al.*, 2001; Mohanty *et al.*, 2004; Sekaric *et al.*, 2004). Applications of silicon micromachines usually involve a dense array of identical meso-scale units on a chip, such as used in the switching of light between optical fibers (Bishop *et al.*, 2001; Aksyuk *et al.*, 2003) or the optical monitoring of the dynamics of a MEMS resonator array driven by tunable electrostatic coupling (Buks and Roukes, 2002; Lifshitz and Cross, 2003).

In the next section, the fabrication of hard and soft nonlinear micromechanical cantilever arrays is described. Starting with the Euler-Bernoulli beam theory in Sec. III, a lumped lattice cantilever model is developed for numerical simulations, which contains both onsite and intersite nonlinearity. The breakup of the large amplitude uniform mode into ILMs by means of a modulational instability is explored with a frequency chirped and with a cw driver. The experimental arrangement for the optical visualization of ILMs is described in Sec. IV. First the harmonic normal modes are measured, and then, using the large amplitude modulational instability, ILMs are produced. Section V deals with the optical manipulation of an ILM by using a laser-induced impurity mode. The low-frequency impurity mode is produced via local laser heating, and its interaction with an ILM in a hard and soft nonlinear lattice is explored. These experimental findings are then followed by numerical simulations of the ILM-optical interaction in Sec. VI. The resulting attractive and repulsive interactions between an ILM and an impurity-induced local mode for both soft and hard nonlinear lattices are presented. In the concluding section, Sec. VII, possible applications to other nonlinear systems in physics and engineering are described. Our discrete cantilever array model that transitions from the Euler-Bernoulli elastic beam theory is presented in the Appendix.

II. CONSTRUCTION OF CANTILEVER ARRAYS

The cantilever arrays are produced by the process of micromachining using standard optical lithography techniques (Fauver *et al.*, 1998; Ilic *et al.*, 2000; Sekaric *et al.*, 2002). A simplified cartoon illustrating the fabrication process for the coupled cantilever array is shown in Figs. 2(a)–2(c). The starting film is a low stress silicon nitride layer on a silicon substrate. After coating with a photoresist mask it is exposed and then etched with a CF_4 plasma in a reactive ion chamber. Next the silicon substrate is undercut using an anisotropic KOH etch, thus releasing the SiN_x cantilevers. A top view of the resulting structure is shown in Fig. 2(d). The width of the overhang (which provides a coupling mechanism between the individual oscillators) is the only dimension that cannot be controlled by lithography. This simple structure and processing reduce fabrication errors and permit the study of nearly identical coupled oscillators. In an actual di-element sample the long and short cantilevers differ in length by about 10%. In a typical sample, the array pitch (i.e., spacing between adjacent cantilevers), the cantilever length, and the length of the overhang are all approximately the same, each about 50 μm.

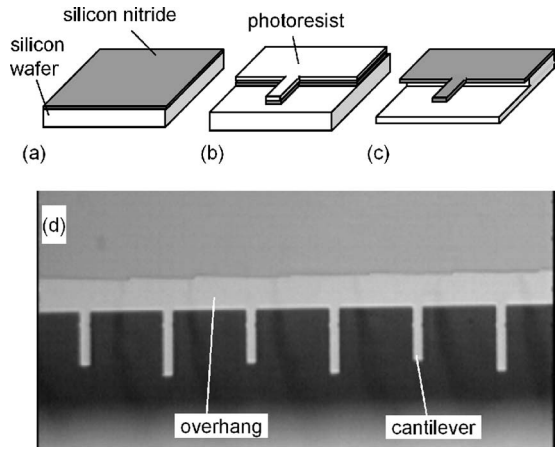

FIG. 2. Fabrication of a micromechanical array with hard nonlinearity. (a) Silicon nitride deposition of 300 nm thickness on a silicon substrate, (b) definition of cantilever geometry by photolithography and CF_4 plasma etching of the nitride layer, and (c) KOH wet etching of the silicon substrate producing the cantilever and the overhang. The length, pitch, and overhang of a di-element array are all roughly the same, on the order of 50 μm. (d) Microscope image of the top view of a finished sample. Bright gray, bare silicon nitride thin film; dark gray, film over silicon substrate.

These fabricated micromechanical structures have a natural hard nonlinearity so that the resonance frequency increases with increasing vibrational amplitude. Hence any ILM will evolve from the highest frequency mode in the linear dispersion curve (Bickham *et al.*, 1992). It will appear above the zone-boundary ($k=\pi/a$) frequency in a mono-element lattice [as illustrated in Fig. 1(b)] and above the zone-center ($k=0$) frequency for the di-element lattice. Our recipe for producing ILMs is first to drive the appropriate uniform mode to large amplitude where it becomes unstable (Kivshar and Peyrard, 1992; Sandusky and Page, 1994) and use this instability to generate ILMs. Hard nonlinearity dictates a di-element array so that the $k=0$ optic mode can be driven uniformly by a piezoelectric transducer (PZT).

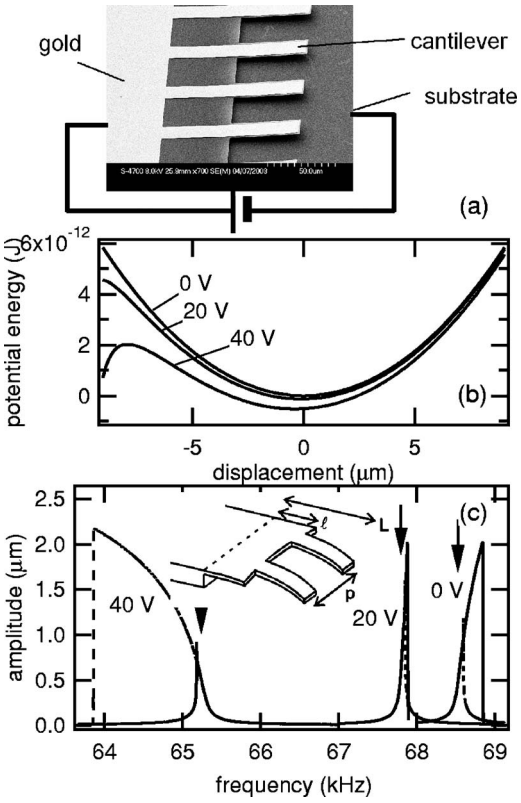

FIG. 3. Fabrication of a micromechanical array with soft nonlinearity. (a) Electron microscope image of a gold-coated mono-element cantilever lattice so that a dc voltage can be applied. The applied bias is used to modify the sign of the lattice nonlinearity. (b) Potential energy of a cantilever for different bias voltages. (c) Frequency-dependent amplitude vs voltage showing both hard and soft nonlinearity for the uniform mode of a mono-element array with the gold electrode. Increasing (solid) and then decreasing (dotted) the driving frequency gives rise to hysteresis in the amplitude response. For 0 V the potential is hard, for 40 V the potential is soft. At 20 V the potential is nearly harmonic. Parameters are listed in Table II, column 3, except now $\alpha=200$ m/s^2.

In order to study a lattice possessing a soft nonlinearity, we must modify the natural hard potential of our system. This is accomplished by first depositing a gold film on the cantilevers and then applying a bias voltage between the gold and the conductive silicon substrate (Younis and Nayfeh, 2003). An electron microscope image of the gold-coated sample is presented in Fig. 3(a). The resulting cantilever potential energies for three different voltage values are shown in Fig. 3(b). The bias voltage introduces both odd and even terms in the cantilever potential. Both introduce soft contributions that counteract the hard quartic potential: odd terms are always soft and the sign for the even terms is negative. The simulation results shown in Fig. 3(c) demonstrate how the applied voltage modifies the nonlinear frequency response of a cantilever. In frame (c) the solid lines correspond to the driving frequency increasing monotonically, while the dotted curves correspond to a decreasing driving frequency.

For no applied bias ($V=0$) the system is in its natural state of a hard nonlinearity. This is clearly demonstrated in Fig. 3(c) where the nonlinear response curve is asymmetric and leaning towards the higher frequencies. An asymmetric response curve that changes depending on whether the frequency is increasing or decreasing (hysteresis) is the signature of a nonlinear oscillator (Cleland, 2003). The fact that this curve leans to higher frequencies means that the resonance frequency of the system increases with increasing vibrational amplitude, i.e., the nonlinearity in the potential is hard.

As the bias voltage increases, the nonlinearity softens. The potential energy curves in Fig. 3(b) are seen to become asymmetric with increasing voltage. Correspondingly, the frequency response curves in Fig. 3(c) show markedly different characteristics. At 20 V the softening of the potential due to the electric field nearly cancels out the natural hard nonlinearity and hence the frequency response is nearly symmetric. At larger voltages, for example, at 40 V, the potential energy becomes even more asymmetric and the frequency response shows a strong soft nonlinear behavior. Applying such a large bias has another physical consequence. Notice that in Fig. 3(b) the potential energy term turns over at large negative amplitude. We found it necessary to increase the gap between the cantilever and the substrate to a distance of 10 μm to keep the cantilevers in large amplitude ILMs from becoming trapped by this electrostatic contribution. If a cantilever touches the oxide-etched clean silicon surface, it is then permanently electrochemically bonded to the surface (stiction) and the introduction of such permanent defects makes the array unusable for further experiments.

III. NUMERICAL SIMULATION STUDIES OF LOCKED ILMs

A. Development of a discrete lattice model

1. A single cantilever

To justify the lumped parameters in Eq. (1) for simulating the dynamics of the cantilever array the effective spring constants must be determined. There are two components to evaluate: the single cantilever and the overhang. Under a set of simplifying assumptions known as Euler-Bernoulli beam theory (Crespo da Silva and Glynn, 1978; Malatkar and Nayfeh, 2003), a continuum equation of motion describing a single cantilever can be derived which contains both hard and soft nonlinearity. The soft nonlinear contribution (inertial nonlinearity) is ignored here since it was not observed in our single micromechanical cantilever experiments. In the Appendix, Sec. 1, it is shown how an equation describing the time-dependent dynamics of a cantilever tip can be obtained from the continuum equation of motion. The result is

$$m\frac{d^2}{dt^2}x(t)+\frac{12.36EI}{L^3}x(t)+\frac{10.11EI}{L^5}x^3(t) = 1.566m\alpha\cos(\Omega t), \tag{2}$$

where $m=\rho AL$ is the cantilever mass, ρ is the cantilever

density, A is the cross-sectional area, L is the length of the cantilever beam, E is Young's modulus of the material, $I=1/(12wh^3)$ is the second moment of inertia (also called the moment of area) (Landau and Lifshitz, 1970) where w is the width and h is the thickness of the beam, α is the acceleration amplitude, and Ω is the external driving frequency. This expression has the form of a Duffing equation (Cleland, 2003). The hard quartic spring constant for the mass and spring model is $k_4 = 10.11EI/L^5$.

To obtain an upper limit on this hard quartic spring constant assume that the cantilever bends at the overhang edge in which case the length L in Eq. (2) would be about 50 μm (see Table II for exact length values for each sample). The other relevant material characteristics in Table II have the values $E=110$ GPa, $h=300$ nm, and $w=15$ μm, which results in the nonlinear onsite spring constant value $k_{4O}=1.2\times10^8$ kg/m^2 s^2.

2. Electric-field-induced soft-onsite nonlinearity of a cantilever

Depending on the applied dc voltage between an Au-coated cantilever and the substrate, the sign of the nonlinearity can be changed from hard to soft (Younis and Nayfeh, 2003). For this geometry the mechanical potential energy of a single cantilever becomes

$$U=\frac{1}{2}k_{2O}x^2+\frac{1}{4}k_{4O}x^4-\frac{1}{2}\varepsilon_0\frac{w(L-l)}{d+x}V^2, \tag{3}$$

where ε_0 is the dielectric constant of free space, $S=w(L-l)$ is the surface area of the cantilever, V is the voltage, d is the gap distance between cantilever and substrate, and x is the cantilever displacement. The mechanical potential energy curves are shown in Fig. 3(b). The equilibrium point decreases as the potential increases and for sufficient cantilever amplitude the tip may reach the substrate and become electrobonded to it. It is important to balance the need for sufficient amplitude so that the nonlinearity plays a role, while at the same time ensuring that the amplitude is small enough so that the equilibrium point remains near zero displacement.

3. Numerical estimate of the hard *intersite* nonlinearity

The actual array consists of cantilevers plus a common overhang region that provides the coupling interaction. To estimate the hard nonlinear intersite coupling consider the zone boundary mode of the mono-element cantilever array (e.g., the $k=0$ opticlike mode of the di-element array). Each cantilever vibrates π out of phase with its neighbor, so that the position of the overhang halfway between two cantilevers remains stationary throughout the motion. Now consider the overhang region in one unit cell extending from one stationary point to the next. The analogous small amplitude sinusoidal motion corresponds to that of a bar with both ends attached to hinges but with the distance between the two hinges fixed. For this bar with both ends fixed the stretching motion, i.e., the hard nonlinearity, is larger than for a bar with one end fixed (cantilever). The nonlinear continuum equation for a bar with both ends fixed is described by Woinowsky-Krieger (1950). The Appendix, Sec. 2, describes how the intersite nonlinear contribution to the cantilever tip equation can be obtained. The result is

$$0.102m_{\text{over}}\frac{d^2}{dt^2}x(t)+0.004\,23\frac{\pi^4h^3EL}{p^3}x(t)+0.000\,831\frac{hE\pi^4L}{p^3}x^3(t)=0. \tag{4}$$

The second and third terms are the linear and nonlinear forces acting on the cantilever tip due to the overhang deformation. The full equation for the cantilever tip vibrating in the zone-boundary mode of a monocantilever lattice is obtained by adding Eqs. (2) and (4). The resulting harmonic parameters can be determined by fitting to the experimentally measured small amplitude dispersion curves. To estimate the relative size of the intersite nonlinear term it is now evaluated using the mass-spring model.

From the model described by Eq. (1), the nonlinear force acting on one cantilever for the opticlike mode of a di-element array (or the zone boundary mode of the mono-element one), where neighboring elements are π out of phase, is

$$F_{4I}=k_{4I}(x_i-x_{i+1})^3+k_{4I}(x_i-x_{i-1})^3=16k_{4I}x^3. \tag{5}$$

Comparing Eqs. (4) and (5) gives an expression for the nonlinear intersite spring constant for the mass-spring model, namely, $k_{4I}=5.19\times10^{-5}(hE\pi^4L/p^3)$. Inserting the parameter values from Table I, column 2 with $E=110$ GPa, gives $k_{4I}=7.29\times10^{10}$ kg/s^2 m^2. In estimating

TABLE I. Experimental parameters for three different micromechanical arrays. The length in parentheses is for the shorter cantilever of the di-element array.

Sample label	I hard	II hard	III soft
Type	di-element	di-element	mono-element
Thickness (nm)	300	300	300
Pitch (μm)	40	65	67
Length (μm)	55 (50)	55 (50)	55
Width (μm)	15	15	15
Total number	248	152	122
Overhang (μm)	67	70	50
Gap (μm)			10
f_4 (kHz)[a]	147.0	136.1	124.29
f_3 (kHz)[a]	143.2	133.0	
f_2 (kHz)[a]	127.7	121.2	
f_1 (kHz)[a]	60.8	72.7	70.72

[a]Resonant frequencies at the upper-zone center, upper-zone boundary, lower-zone center, and lower-zone boundary. For the mono-element-type arrays, only two frequencies are specified.

this coupling strength only the stretching of the overhang has been counted and the smaller bending contribution has been ignored. The important result is that the intersite nonlinearity given by Eq. (5) is much larger than the onsite cantilever nonlinearity given by Eq. (2); hence, according to Fig. 1(b) strongly localized ILMs are to be expected.

4. Complete mass-spring model for the di-element cantilever array

The effective spring constants described above have been incorporated into the mass-spring model for the di-element array. One additional contribution comes from long vibrational wavelengths at lower frequencies in the overhang region. This effect mimics a long-range interaction in the mass-spring model and causes the bandwidth of the acousticlike branch to differ from that of the opticlike branch. The final expression for a vibrating cantilever, which includes all of these contributions plus a frictional term, is

$$m_i\frac{d^2x_i}{dt}+\frac{m_i}{\tau}\frac{dx_i}{dt}+k_{2Oi}x_i+k_{4Oi}x_i^3 + \sum_j k_{2I}^{(j)}(2x_i-x_{i+j}-x_{i-j}) + k_{4I}[(x_i-x_{i+1})^3+(x_i-x_{i-1})^3] = m_i\alpha\cos(\Omega t), \quad (6)$$

where the index i (odd) refers to a long cantilever and i (even) to a short one. By numerically fitting the linearized version of Eq. (6) to the experimentally measured linear-response data the model with sixth-nearest-neighbor interactions describes the full di-element dispersion curve. The right-hand side of Eq. (6) is defined below Eq. (2).

B. ILM simulation experiments

To simulate the nonlinear array dynamics the coupled equations of motion represented by Eq. (6) are integrated forward in time using a fourth-order Runge-Kutta routine (Press *et al.*, 1992). Starting with all oscillators at rest, the large amplitude driver is initiated with its frequency at the top of the opticlike branch and is then chirped to higher frequency with time to provide enough vibrational amplitude to induce a modulational instability (Dauxois and Peyrard, 1993; Sandusky and Page, 1994; Rössler and Page, 2000) of the uniform mode, which then leads to ILM generation. At each time step of the integration a small amplitude noise field is applied as an external driving force in order to simulate the effects of random vibrational noise. The cantilever displacement is recorded and then used to calculate energy. At the end of such a frequency chirp, the driver frequency is far above the top of the linear opticlike band, and only feeds energy into ILMs.

Simulation results showing the creation, interaction, and destruction of ILMs are summarized in Fig. 4. This lattice consists of 248 cantilevers with hard nonlinearity.

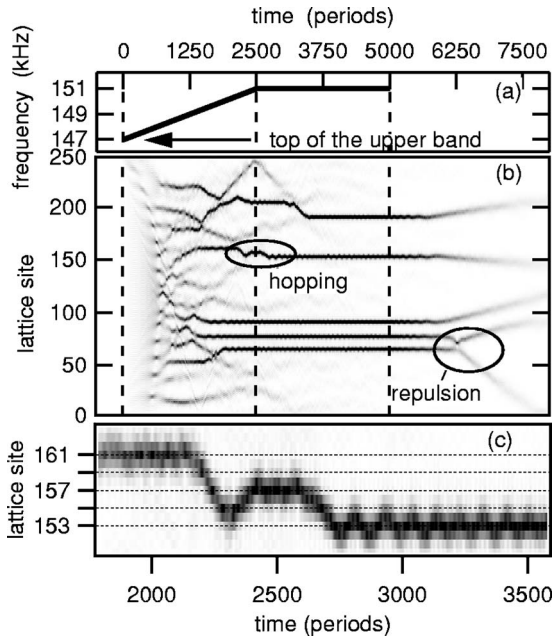

FIG. 4. A simulation of ILM production, dynamics, and decay for a di-element array with hard anharmonicity. Cantilever simulation parameters are listed in Table II, column 1. (a) Driver frequency as a function of time for this simulation. The driver is on from $t=0$ to 5000 periods. The driver frequency starts just below the optic mode frequency f_4, increases up to $1.027f_4$ linearly until 2500 periods, and then remains at that frequency. The amplitudes of the ILMs increase with time until the end of the chirp. The magnitude of the acceleration is kept constant, at $\alpha=1.4\times10^4$ m/s^2. (b) A density plot of the vibrational energy distribution vs time. Dark regions identify large amplitude localized modes. During the time that the cw driver is on five locked stationary ILMs appear. ILM hopping is identified in the left oval marker. Once the driver is turned off, the ILM amplitude decreases and as its width increases it becomes unpinned from a particular lattice site. ILMs are seen to interact and repel one another. (c) Magnified image of the ILM hopping event identified in the oval in (b). The resting position is always on a short lattice site (horizontal dotted lines). Other observations: When the ILM amplitude is small, $t<2500$ periods, the lattice pinning effect is weak and ILM collisions permit them to hop among stable sites. When the ILM amplitude becomes large the pinning effect is strong, and an ILM oscillates about a particular trapping site.

First the driver is chirped to larger frequencies above the opticlike branch for 2500 periods then left at a fixed frequency for another 2500 periods and finally turned off, as illustrated in Fig. 4(a). Figure 4(b) shows an energy density plot for each cantilever site (high energy =dark) as a function of time for a typical simulation experiment. During the chirping phase of the driver many moving ILMs are created, which then coalesce into a small number of ILMs. The ILMs that are not on speaking terms with the driver die out after about 2000 periods of oscillation. In this particular simulation, five modes can be identified that persist into the cw region of the driver. These ILMs have their frequencies locked to the driver and, because of the large amplitude, nonlin-

earity traps them at particular lattice sites. This synchronization with the driver provides a continuous transfer of energy to the ILMs, which keeps them pinned at particular lattice sites and prevents them from decaying. Other ILMs fail to frequency lock to the driver in the cw region, and hence ultimately decay after a time lapse of ~2600 periods. Once the driver has been turned off, the five locked states persist for another 1300 periods, about the same interval as the natural lifetime, and then they decay. The two ILMs in the oval labeled "repulsion" are close enough together so that once amplitude decay begins, they become unpinned and a strong repulsion is observed. A somewhat weaker repulsion is felt by ILMs farther apart and they all move through the lattice as they decay.

Figure 4(c) shows a magnified image of the hopping event by the other oval in Fig. 4(b). Hopping by a single ILM occurs because of the pinning effect due to the energy difference between the single-peaked, odd-site centered eigenvector and the double-peaked, even-site centered eigenvector for the di-element array. Because the odd-site centered mode is more stable in a di-element array, the ILM remains for a longer time at the odd site. Due to the pinning effect, the ILM can remain stable at a particular lattice site, even in the presence of small perturbations. Once the perturbations grow large enough to overcome the pinning potential barrier, the ILMs may begin to hop between odd sites. It is the other decaying ILMs in Fig. 4(b) (at about 2500 periods) that are the source of the perturbation that leads to the hopping event displayed in Fig. 4(c). The pinning effect is enhanced for large ILM amplitudes. By the end of the chirp, the ILM amplitudes are sufficiently large so that they are stable at their respective sites. Once an ILM has become pinned at a particular site, it will initially oscillate laterally around the stable odd lattice site due to the lateral trajectory that existed when the ILM entered the site. Similar oscillations of ILMs have been predicted (Sandusky *et al.*, 1992).

To explore the development of locked ILMs from another perspective, the double Fourier transform of the cantilever motion over a specific time interval is taken. The (space, time) data result in a new data set in reciprocal space (wave vector, frequency). The resulting time developments of excitations both in real space and in k space are shown in Fig. 5. The same driving conditions are used as those in Fig. 4. Of course the initial noise field is not the same. The frequency chirp ($f_a \rightarrow 1.027 f_a$) lasts for 2500 periods [left dashed vertical line in (a)]. At longer times only one locked ILM appears. The cw driver is turned off at 5000 periods [right dashed vertical line in (a)]. By space-time Fourier transforming the displacement over the different time intervals identified by the double headed arrows: a, b, c, d, e, f, and g, in Fig. 5(a), the (ω,k) excitation plots shown in frames (b)–(g) are obtained. The lowest frequency curved trace in these six frames identifies the linear dispersion curve of the opticlike branch for the di-element cantilever array. Figures 5(b) and 5(c) show time cuts taken during the chirp. The position of the nonlinear dispersion curve and the

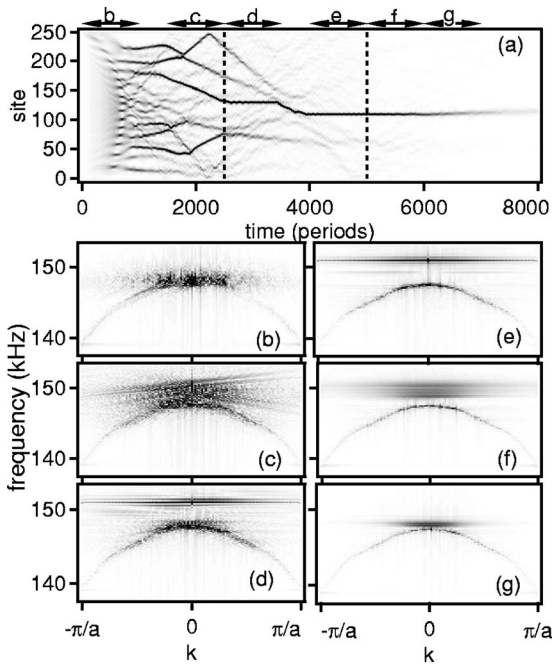

FIG. 5. Evolution of ILM energy vs time in both real and reciprocal space. (a) Spatial distribution of vibrational energy density vs time in real space. The simulation parameters are the same as for Fig. 4. (b)–(g) Time-space Fourier transform of the displacement for a number of time windows. The time windows for these frames are indicated by the letters b through g above frame (a). The ILM time development during the initial chirped driver are shown in frames (b) and (c), frame (c) is particularly interesting since it shows nonhorizontal straight lines associated with running ILMs as well as excitations in the top of the optic branch. The straight line slope gives the ILM velocity. (d),(e) The horizontal line associated with the locked state, and after the cw driver is turned off the decaying ILM state is shown in (f) and (g).

interference between different ILMs as well as their translational motion can be seen in Fig. 5(c). The early and late signature stages of a single locked ILM state appear in Figs. 5(d) and 5(e). The latter case represents steady state. Figures 5(f) and 5(g) identify the decaying state. The time evolution of Fig. 5 shows that initially the region above the linear dispersion curve is almost uniformly excited in k space [Fig. 5(b)], while in real space there are many different levels of excitations and localized excitation speeds. By the middle of the chirp, several strong tracks, characteristic of ILMs, emerge in the k-space representation [Fig. 5(c)]. In the initial stage after the chirp, one strong horizontal excitation is accompanied by relatively weak decaying ILMs as shown in Fig. 5(d). The vertical line at the 151 kHz, $k=0$ point, in Figs. 5(d) and 5(e), is a real feature that occurs at the driver frequency. It comes about because the center of the locked ILM is in phase with the driver, while the rest of the lattice is out of phase. After the pulse is turned off, the ILM loses energy and its frequency decreases as shown in Figs. 5(f) and 5(g).

C. Summary from numerical studies

The general picture from simulations is that initially a number of moving localized modes are created, but that there are only very few modes that grow in amplitude and survive until the end of the chirp, and even fewer survive until the end of the cw interval. It has been determined that these ILMs are frequency locked to the driver. In this way sufficient energy can be transferred to maintain their strongly localized state and fixed vibrational amplitude. Other ILMs decay if they fail to lock their frequency and phase to the driver. A theoretical work (Rössler and Page, 1995) has reported a locked in-phase driven single-peaked ILM with out-of-phase background for a realistic anharmonic potential. Their description is somewhat similar to what is observed here. Our simulations confirm that the mobility of localized modes decreases with increasing amplitude (Bickham *et al.*, 1992), and if the amplitude becomes large enough, the localized mode is trapped at a lattice site (Bang and Peyrard, 1995). Although the nonlinear lattice does not support a Peierls-Nabarro potential (Kivshar and Campbell, 1993; Cai *et al.*, 1994) due to the presence of internal degrees of freedom (Flach *et al.*, 1993; Flach and Willis, 1994), a pinning potential of some kind still appears to be a valid concept.

IV. EXPERIMENTAL STUDIES OF ILMs

A. Visualization of micromechanical ILMs

The procedure for creating ILMs in a di-element array with hard nonlinearity is to drive the uniform optic mode to large amplitude where it becomes unstable (Kivshar and Peyrard, 1992; Sandusky *et al.*, 1992; Daumont *et al.*, 1997; Rössler and Page, 1997) and breaks up into localized excitations. To visually inspect the development of ILMs when the cantilevers are driven to large amplitude, a diode laser is focused with a cylindrical lens into a line along the static cantilever array as illustrated in Fig. 6(a). The reflected beam is then imaged on the 1D charge-coupled-device (CCD) camera. As the vibration of a cantilever grows, the reflected laser beam increasingly *misses* the 1D CCD camera, and the image of that particular cantilever grows darker.

Figure 6(b) shows the different elements in the actual experimental layout. The sample in a vacuum chamber is mounted to a PZT, which uniformly shakes the entire sample so that the cantilever array experiences a common acceleration. The PZT is driven with a voltage-controlled oscillator for variable or constant frequency operation. The switch and ramp generator are synchronized to the camera using a pulse generator. Images are captured with a computer, which is triggered by the pulse generator (Sato, Hubbard, English, *et al.*, 2003). The speed of the camera, about 18 kHz, is insufficient to monitor the sinusoidal motion of the cantilevers, which is on the order of 100 kHz; however, it can measure the vibrational envelope. Further, this rate is sufficient to observe the speed of the fastest traveling localized excitations that can be produced. Consequently, the capturing speed of the camera is fast enough to observe both the lateral motion of a localized mode and its time development. This relatively straightforward observational method permits a systematic monitoring of the excitation pattern and its interaction with a driver.

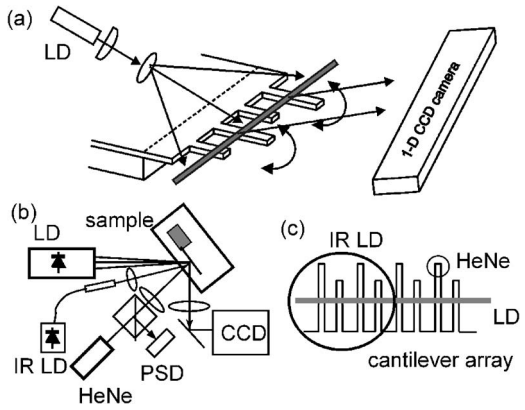

FIG. 6. Experimental setup for observing ILMs. (a) A low power laser beam is used to probe the motion of the cantilevers. A cylindrical lens produces a line focus on the tips of the cantilevers. The reflected image is directed by a lens (not shown) onto a 1D CCD camera. The image from a highly excited cantilever will increasingly miss the CCD producing a dark spot. (b) Complete optical arrangement for three different kinds of measurements including the linear frequency response of the system, the ILM observing setup shown in (a), and the production of an optically induced impurity mode. The sample in vacuum is driven by a piezoelectric transducer (PZT). A HeNe beam is focused onto a cantilever, reflected from it, and directed to a position sensitive detector to measure the linear vibrational response. A fiber pigtailed infrared laser diode is used to locally heat a few elements and produce a movable, gap impurity mode in the cantilever array. (c) Schematic representation of the three kinds of laser images on a di-element cantilever surface.

B. Linear frequency response measurement and normal modes

The optical arrangement used to measure the linear and nonlinear spectral response of a cantilever array is also shown in Fig. 6(b). A low power (~2 mW) HeNe laser is focused onto the tip of the desired cantilever. The combination of a variable frequency signal generator, amplifier, and adjustable attenuator is used to drive the PZT. The resulting deflection of the laser beam from the individually selected oscillating cantilever is measured by a position sensitive detector (PSD). A quasistatic sweep procedure is then used in which the driver frequency is incremented in small steps (typically about 50 Hz) to plot out the vibrational amplitude versus driving frequency spectrum.

The small oscillation opticlike and acousticlike normal modes of a di-element array containing 152 cantilevers are shown in Figs. 7(a) and 7(b). The curves labeled OFF are the normal mode spectra in the absence of any ex-

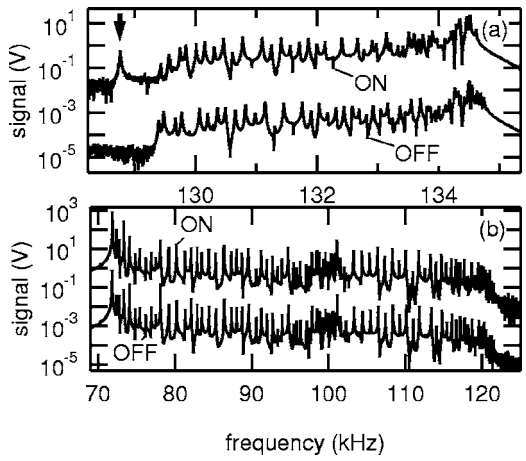

FIG. 7. Measured frequency spectrum produced by the linear normal modes of a di-element cantilever array. OFF: The response spectra of one cantilever for (a) opticlike and (b) acousticlike bands are shown. ON: The spectra for a local laser-heated case described in Sec. V is also shown (shifted up for clarity). Here a linear impurity mode is created below the optic branch, as indicated by the arrow. After Sato *et al.*, 2004.

ternal perturbation besides the PZT driver. (The curves labeled ON will be discussed in Sec. V.B, where the laser interaction with ILMs is considered.) The ability of the uniform driver to couple to these nonuniform extended modes is due to the finite size of the lattice. The boundary conditions produce even- and odd-type modes so in order to identify all the modes of the system the experiment is repeated at a few different cantilevers, some at the edge and some near the middle of the array. Note that the acousticlike band (b) is much wider (~50 kHz) than the opticlike band (a) (~5 kHz) demonstrating that the overhang acts like a long-range coupler between cantilevers.

C. Large amplitude modulational instability and ILM development

Examples of cantilever amplitude versus time for two different cantilever arrays are shown in Fig. 8. For a large amplitude driver three independent but sequential time-dependent response measurements, (a)–(c), are shown for a 248 array and a second set of three, (d)–(f) are shown for a 152 array. The initial cantilever positions are identified by the horizontal lines to the left of the *t*

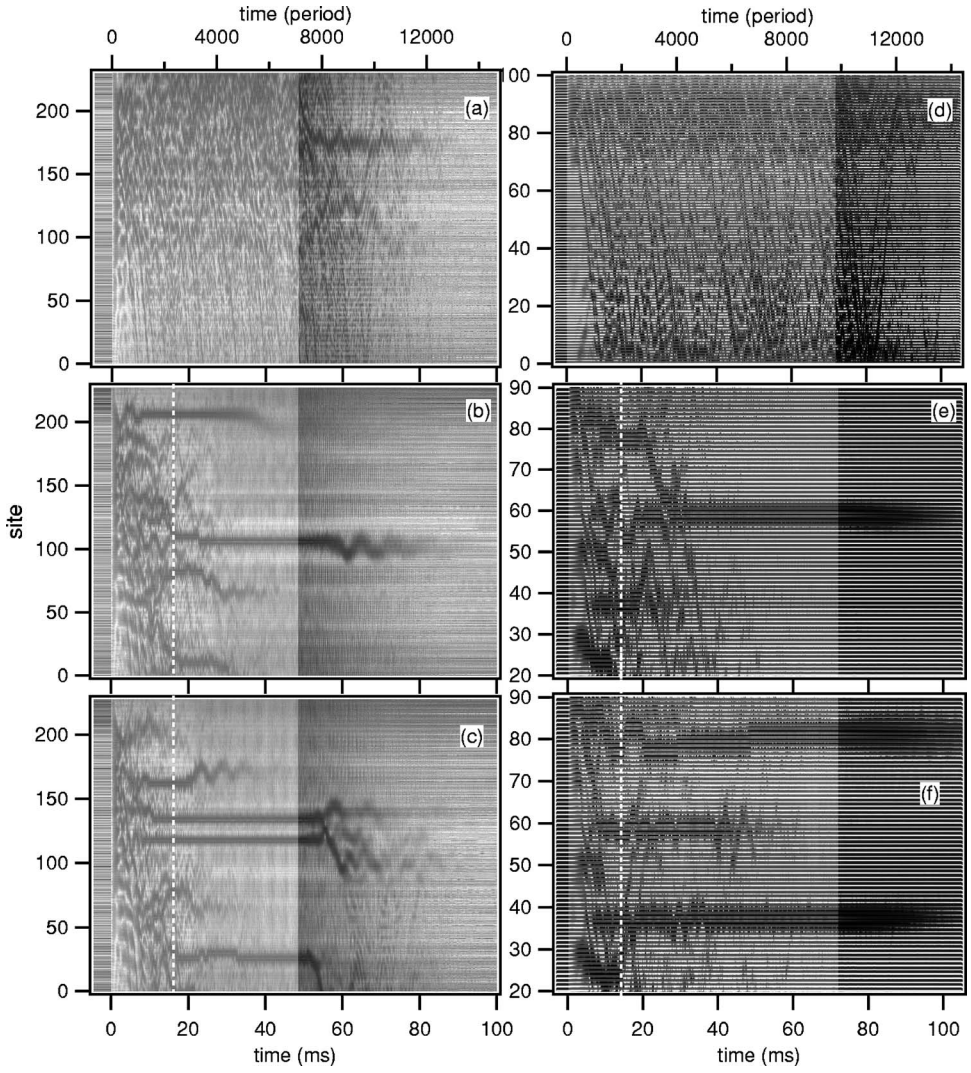

FIG. 8. Cantilever excitation vs time showing the production, interaction, and decay of ILMs. These experimental results for (a)–(c) 248-element and (d)–(f) 152-element arrays are taken with the 1D CCD camera. (a) The PZT driver has a fixed frequency at the top of the optic branch. Running modes are produced. (b),(c) Identical starting conditions. The PZT frequency is now chirped from 0.9986 to 1.016 times the optic branch frequency. (d) The driver frequency is again fixed at the top of the optic branch (136.3 kHz). In (e) and (f) the driver frequency is chirped from 1.000 to 1.011 times the optic branch frequency. (e),(f) Identical starting conditions. The chirp ends at 16.2 ms for (b) and (c), 14.2 ms for (e) and (f). The dark regions identify localized excitations. The lighter regions correspond to times when the driver is on. Some localized excitations become trapped during the cw phase. The driver duration is 48.9 ms for (a)–(c) and 72.7 ms for (d)–(f).

=0 time marker. The darker region of the pictures beyond 48.9 ms for (a)–(c) and 72.2 ms for (d)–(f) indicates that the cw driver is turned off. The CCD camera images a portion of the sample, which is 230 cantilevers for (a)–(c) and 100 cantilevers for (d)–(f). In Sec. IV.A it was described that the camera records darkness when a cantilever vibrates with large amplitude. Hence the individual dark tracks versus time identify the positions of large amplitude localized excitations.

Figure 8(a) shows the cantilever excitation versus time when the high-power, PZT driver frequency is fixed at the top of the optic band. Many dark tracks are visible but no particular pattern is evident. The appearance of the dark tracks indicates that some of the cantilevers are highly excited. The lack of an apparent pattern indicates that many running modes are present and simply superimposed upon each other. In Figs. 8(b) and 8(c) the driver is chirped from the top of the optic branch to higher frequency, up to 1.016 times that value over a time interval of 16.2 ms. The initial condition in Figs. 8(b) and 8(c) is exactly the same yet different localization results are observed. This is to be expected for a process initiated by random noise and not by impurities in the lattice. Some moving ILMs form during this chirp phase. At longer times between 16.2 and 48.9 ms, with a cw driver some ILMs continue to receive energy while others die out. At some point a few large amplitude ILMs become trapped at specific lattice sites. This can be seen around lattice site 100 in Fig. 8(b) and at three locations, namely, 25, 117, and 133 in Fig. 8(c). After the driver is turned off at time=48.9 ms, the trapped ILMs decay. In a number of cases the decaying ILMs are observed to undergo lateral oscillations about their equilibrium position, perhaps due to Bloch oscillations (Kosevich, 2003). These oscillations could occur when a static force applied to a mobile ILM gives rise to Bragg reflections. The initial vibrational patterns shown in Figs. 8(a) and 8(b) demonstrate that the 248-cantilever sample has a slight gradient across the sample in its mechanical parameters while the 152-element sample does not. Hence an ILM would feel a static lateral force in the former case but not in the latter.

Similar localization phenomena can be seen with the 152-cantilever array as shown in Figs. 8(d)–8(f). The running modes are generated when the driver frequency is fixed at the top of the optic branch [Fig. 8(d)]. However, when the driver frequency is chirped up from the top of the optic branch, moving ILMs are generated. Some then become pinned and locked during the cw driver mode. The driver amplitude for Figs. 8(b) and 8(c) is larger than in Figs. 8(e) and 8(f) and the somewhat diffuse background excitations observed in the former case are missing in the latter one. The more uniform distribution of running plane wave modes in Fig. 8(d) compared to Fig. 8(a) is an indication that the fabricated array of cantilevers is more uniform in this case. This 152 cantilever sample is used in the ILM-laser interaction experiment described in Sec. V.C.

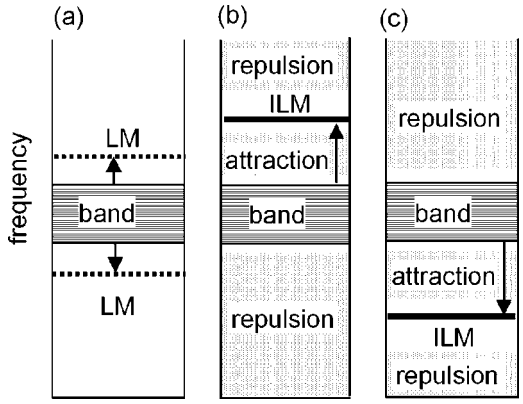

FIG. 9. Summary of the impurity mode-ILM interaction results obtained from different simulations. (a) Linear system. A local mode (LM) appears above or below the plane-wave band states depending on the sign of the linear onsite spring constant change. (b) For the nonlinear array with hard nonlinearity a stationary ILM is created above the band states. When the impurity mode is either below the band states or above the ILM frequency, the ILM is repelled, as represented by the shaded regions. When the impurity mode is above the band states but below the ILM frequency, the ILM is attracted. (c) For the nonlinear array with soft anharmonicity the ILM appears below the band states. The conditions for the ILM repulsion or attraction interaction are now inverted with respect to case (b).

V. OPTICAL MANIPULATION OF ILMs

A. Logic and experimental arrangement

It is known from a variety of simulation studies (Bickham *et al.*, 1993; Kiselev *et al.*, 1994; Sato *et al.*, 2004) that ILMs do interact with localized impurity modes. Numerically all possibilities for a linear force constant impurity mode interacting with an ILM have been explored for both a hard nonlinear and a soft nonlinear lattice. These findings, as well as those described in Sec. V, are summarized schematically in Fig. 9. For reference Fig. 9(a) presents the local mode (LM) frequencies with respect to a bounded plane wave band produced by an onsite force constant defect increase or decrease in a harmonic host lattice. Figure 9(b) shows the ILM-impurity mode interaction results for a lattice with a hard nonlinearity. The high-frequency ILM (solid line) will be repulsed from a nearby linear impurity mode below the host band or above the ILM but attracted to an impurity mode which is above the host band but below the ILM. Figure 9(c) presents the corresponding soft nonlinearity case. Now the low-frequency ILM (solid line) is repulsed from a nearby high-frequency impurity mode above the host band and also repulsed from one below the ILM frequency. The attractive region is above the ILM frequency but below the host band. Of the different cases presented here the most interesting is the region of attraction. But since our local heating technique, to be described below, always produces an impurity mode below the optic branch, it is in the repulsive region of the hard nonlinear lattice, case (b). Since the

two-body potentials that characterize atomic lattices always produce soft vibrational nonlinearity, the attractive region presented in case (c) is particularly relevant for condensed-matter nonlinear lattices and we shall describe experiments relevant to this case as well.

Because ILMs can appear at random places in the lattice the experimental goal here is to introduce "special" impurity modes and examine how they can be used to manipulate ILMs. Local cantilever heating produced by a strongly focused IR laser is used to produce a portable impurity mode which can be brought within the range of an ILM by simply moving the laser spot. The experimental configuration shown in Fig. 6 is only slightly different from that used earlier by Sato, Hubbard, Sievers, *et al.* (2003). Again a laser-line illuminator coupled to a 1D CCD camera is used to monitor the evolution of the excitation pattern of the entire lattice in real time. However, to study the interaction between a laser-induced impurity and an ILM, the new component is a fiber-coupled infrared diode laser labeled IR LD in Fig. 6(b), which can be focused onto a small number of cantilevers along the array. Its spot size is about 200 μm. Figure 6(c) shows the relative spot sizes on the array for the different lasers. Heating the silicon nitride cantilevers has the effect of decreasing Young's modulus, and hence lowering the natural resonance frequency (Buser and de Rooij, 1989; Rouxel *et al.*, 2002). Since only a few cantilevers are affected by this technique, an induced localized impurity mode is created which can then be controllably moved throughout the lattice.

B. Observation and manipulation of ILMs in a hard nonlinear array

To demonstrate that an impurity mode can be produced in the linear spectrum by local laser heating, a weak HeNe probe laser is focused a few lattice sites away from the IR laser (50–100 mW) spot. The dielement cantilever linear-response spectra are then measured by monitoring the probe laser while sweeping the PZT frequency at small amplitude, both with the heating-laser ON and with it OFF. The experimental mode spectra for the optic and acoustic bands for both cases are shown as the spectra in Figs. 7(a) and 7(b). When the heating laser is ON there is an isolated spectral feature below the narrow optic band [identified by the arrow in Fig. 7(a)], indicating the formation of a linear impurity mode in the gap between the optic and acoustic branches. Because of the much larger bandwidth of the acoustic branch, the acousticlike local mode is much closer to the bottom of the band and is not observed in Fig. 7(b).

Figure 10(a) shows the repulsive interaction between an ILM and an impurity mode produced by laser heating. The periodic horizontal white lines identify the stationary cantilever positions. First an ILM locked to the driver is identified (dark horizontal trace at site 73 for the first few ms), then the focused IR laser spot is moved to one side (site 76) of the ILM (broad horizontal white trace). The laser current is then gradually increased until

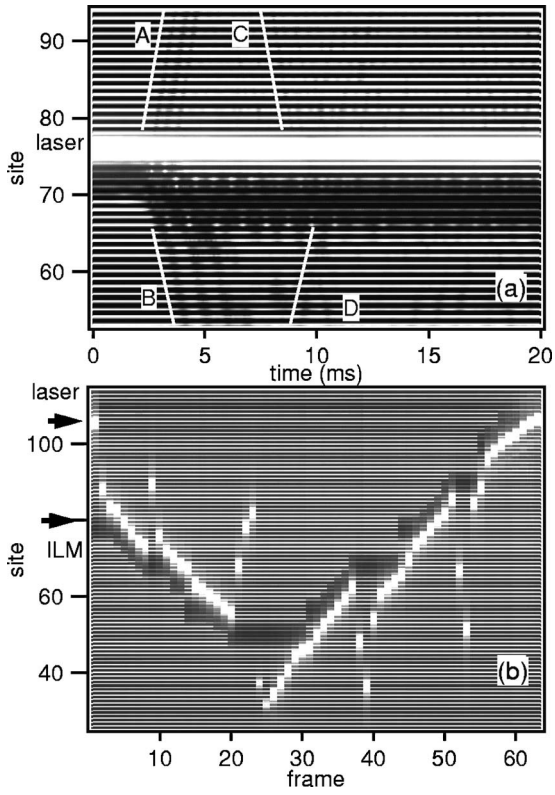

FIG. 10. Laser manipulation of an ILM in an array with hard anharmonicity. (a) Experimental observation of a laser-induced ILM hopping event. Periodic horizontal white lines are images of stationary cantilevers. The dark ILM location is centered at site 73 and the white laser spot is located at site 76. The laser spot is placed nearby a locked ILM and then the IR laser power is gradually increased. When an ILM hops away from the laser spot, it is accompanied by wave-packet emission, as labeled by A and B. Reflected waves from the edges are seen to the right of C and the left of D. The canted white lines are guides to eye of the traveling waves. The speed of these waves are 16.3×10^3, 12.8×10^3, 16.2×10^3, and 12.3×10^3 (p/sec) for A, B, C, and D, respectively, where p is the cantilever pitch. An ILM is stable at shorter cantilever sites (odd numbered sites in this figure). When one hops onto such a site its lateral momentum produces an oscillation that decays with time. (b) Successive manipulation of the ILM. The images are constructed from a number of chronologically ordered pictures. The two arrows at sites 105 and 78 indicate the initial locations of the laser spot and the ILM, respectively. The darkest stripe in each frame corresponds to a highly excited ILM. The white rectangles identify the heating laser spot, which produces a linear impurity mode. As the laser spot approaches, the ILM is repelled and hops away. When the laser spot is far removed, the ILM remains fixed as shown in the frames around 10, 40, and 52. When the laser power is low, it can pass through the ILM without interaction (around frame 23). At the last frame, the ILM was pushed against an impurity site near the end of the array, and disappeared.

the ILM hops (at about 2.5 ms). If the repulsive interaction is strong enough to overcome the pinning effect, the ILM becomes unstable at the original site and finds another stable site. Here, the ILM hops to the second nearest stable site. Several wave packets are emitted during

the hopping event (dark canted lines near A and B). (The canted white lines are added as a guide to the eye.) Wave packets reflected from the array boundaries are located by the markers C and D. Interestingly the ILM oscillates laterally about its new steady-state position as though it was a trapped particle. Although the ILM loses some energy due to this wave-packet emission, it recovers and remains locked to the driver with the same spatial shape after the event as before.

Figure 10(b) illustrates optical manipulation by means of the repulsive interaction using the same process shown in Fig. 10(a). The finely spaced horizontal lines are images of individual cantilevers. The narrow dark region in the first frame (a few ms long) shows the starting point for a stationary, locked ILM. The white rectangles identify the IR laser spot in different frames. The initial locations of the laser spot and the ILM are indicated in the figure by arrows. The ILM is repelled when the laser spot is placed next to its envelope. At about frame 4 the ILM moves away from the laser spot with a hopping motion. Once the ILM hops, it is stable at this new position even if the laser spot is then moved far away (see frames 10, 40, and 52). The ILM can be moved to any location in the lattice using this method. Residual manufacturing impurity effects exist around frames 14 and 44 so that the ILM hops a large distance at these locations. Weak laser power produces no effect on the ILM, even when the spot is swept through it (see the frames near 23). Finally at about frame 60 the ILM vanishes when it is pushed up against an impurity mode near the end of the array. This last observation indicates that it is possible to destroy ILMs at will. These laser-induced impurity mode observations are consistent with simulations.

C. Demonstration of an attractive interaction and dynamical energy tweezing

An array with soft nonlinearity is an important component for the possible extension of these manipulation ideas to nonlinear atomic lattices. As outlined in Sec. III.A.2 and illustrated in Fig. 3 such a micromechanical array can be produced. Since the ILM will now drop out of the bottom of the band only a mono-element lattice is necessary to examine this case experimentally. Such data demonstrating the attractive interaction between an impurity mode and an ILM for the soft nonlinear array are shown in Fig. 11. Again the dark region represents the nearly pinned ILM and the white spot the impurity mode produced by local laser heating. The initial locations of the ILM and the laser spot are indicated in the figure with arrows. As the white spot approaches the stationary ILM frame by frame, not until frame 5 is the ILM attracted and captured. This occurs even though the laser spot has not yet reached the envelope of the ILM. (A similar effect observed in the simulations is described in Sec. VI.B.) Once the ILM is captured, it follows the motion of the laser spot. Note that at frames 10, 18, and 21, the ILM remains in place even though the heating laser is turned off. Because of the large bandwidth of this particular coupled cantilever design a strong PZT excitation is required to separate out a locked ILM. For this reason a background of running modes is conspicuous and, unlike Fig. 10, the horizontal lines of the remaining stationary cantilevers cannot be seen here. Since this ILM envelope is oscillating about its equilibrium position, the pinning phenomenon is effectively weaker and the ILM moves more easily than the one shown in Fig. 10(b).

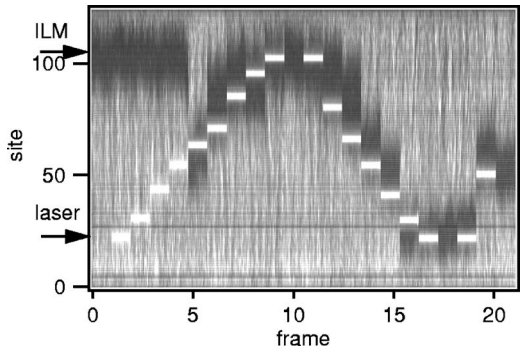

FIG. 11. Observed laser manipulation of an ILM in a soft nonlinear lattice. Demonstration of an attractive interaction for a wide linear bandwidth, soft nonlinear mono-element array. The two arrows identify the initial location of the ILM and the laser spot. As the laser spot approaches an ILM, it is attracted and captured by the impurity mode, see frame 5. As the laser spot moves, the ILM moves with it. When the laser is turned off, the ILM stays in a fixed position (frames 10, 18, and 21). Due to the larger bandwidth of the lattice, the size of an ILM is wider than in the case of the hard nonlinear lattice case. Driving the soft mono-element wide bandwidth array also generates running wave packets, which appear as the noisy line structure throughout the figure. After Sato *et al.*, 2004.

VI. SIMULATIONS OF THE ILM-OPTICAL INTERACTION

A. Interaction between linear impurity modes and ILMs in a hard nonlinear lattice

In simulations, the effect of a laser-heated spot at a specific location on the array is created through the simple modification of one or more onsite spring constants. Decreasing the linear spring constant produces a low-frequency local vibrational mode in agreement with the observed cantilever heating in a lattice. However, ILMs based on the model described by Eq. (6) have narrower widths (either three or five cantilever sites) than observed in experiment. Due to this strong localization, an impurity has to be very close to the center of an ILM to produce an effect. Since the heating effect in the linear spectrum is more conspicuous in the upper branch than the lower one, the impurity is introduced on the shorter cantilever site. Thus to study the manipulation of an ILM by an impurity mode the initial conditions are (i) a single impurity placed at the short cantilever site next to the ILM site centered on a short cantilever site and (ii) a uniform driver frequency 1.0138 above the optic-like band of the di-element array.

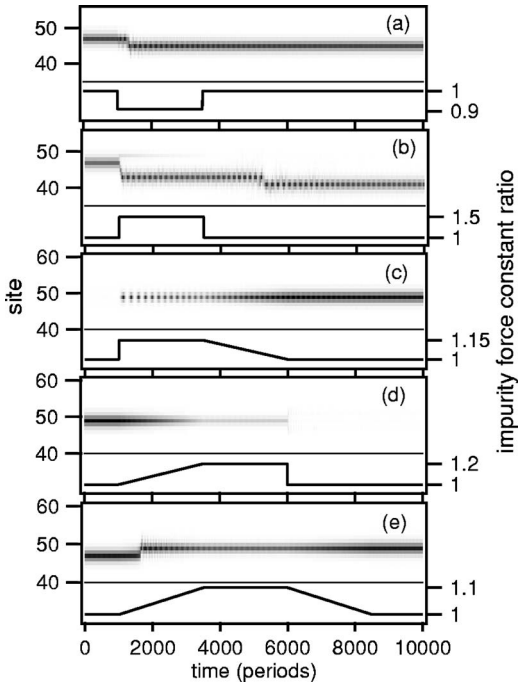

FIG. 12. Simulated time-dependent manipulation of an ILM by an optically induced impurity mode. One linear impurity is placed at lattice site 49 and its onsite spring constant k_{2O} is changed to a defect spring constant with the impurity force constant ratio changing with time as shown in the lower trace of each panel. The energy density of the resulting ILM in the lattice is the upper feature in each panel. Different kinds of ILM manipulation are then demonstrated: (a) Repulsion with a low-frequency impurity mode, (b) repulsion with a high-frequency impurity mode, (c) seeding an ILM using a high-frequency impurity mode, (d) destruction of an ILM using a high-frequency impurity mode, and (e) capturing or tweezing an ILM with a low-frequency impurity mode. Parameters are listed in Table II, column 2.

Figure 12(a) demonstrates the repulsive interaction on an ILM that occurs when a low-frequency impurity mode is nearby. The lower trace in this figure gives the relative spring constant of the impurity as a function of time. The upper trace shows the energy density trace of the ILM. An ILM is originally located at site 47, and one impurity spring constant ($0.91k_{2O}$) is placed at site 49 suddenly at $t=1000$ periods. The ILM moves away from the impurity to a new site at about $t=1300$ periods, and remains at the new position even when the impurity is removed at $t=3500$ periods. The actual hop occurs 100 or more periods after the impurity is introduced. Placing the impurity nearby induces lateral oscillation in the ILM and when the lateral oscillation is large enough to overcome the pinning effect, the ILM hops. In addition, an amplitude modulation (AM) [see the pulsing trajectory in Fig. 12(a)] of the ILM appears as soon as the impurity is introduced. It appears that the lateral oscillation of the ILM is excited by a combination of the AM and the impurity, which breaks the ILM symmetry.

So far in experiments, we can only produce a low-frequency impurity mode; however, there is no such restriction in simulations. Figure 12(b) shows another case of the repulsive interaction with a spring impurity of $1.50k_{2O}$, where a high-frequency impurity mode is placed at the same location as in Fig. 12(a). In this case, the impurity mode frequency is much higher than the driver frequency. The dotted pattern after the placement of the impurity is due to an AM of the ILM vibration, which causes an oscillation of its energy with the period of the dots. This AM pattern is more pronounced than in case (a) above. The decay time of the AM structure is much longer than the damping rate (1200 periods). An interesting phenomenon happened near $t=5000$ periods, the ILM moves again in the absence of any additional perturbation. However, unlike the first case, here the lateral oscillation amplitude becomes smaller as time passes. It is replaced by an increasing amplitude oscillation of the total ILM shape after the impurity is removed, and hopping happens when the amplitude is at one of the minima of the AM oscillation. This delay is probably caused by a parametric amplification process, i.e., the AM oscillation is amplified by the driver locked ILM, which acts as the pump.

Figure 12(c) illustrates how an ILM can be generated by a high-frequency impurity mode (spring constant $1.20k_{2O}$) which has the same frequency as the driver. When the impurity is inserted at $t=1000$ periods, the impurity mode resonates with the driver; however, its amplitude is not large since the nonlinear spring constant causes the actual resonance to occur at much higher frequencies. If the impurity linear spring constant value is returned adiabatically to the lattice value then the amplitude at this spatial location gradually increases. When the impurity vanishes, a new ILM remains at the "virtual" impurity site. The role of the linear spring constant impurity in producing localization is gradually replaced by a virtual impurity that involves an effective hard nonlinear spring constant.

Using the same high-frequency impurity mode as in Fig. 12(c), an ILM can be destroyed, as shown in Fig. 12(d). Here, a linear spring constant impurity is gradually turned on at the ILM site. As the impurity mode frequency increases, the amplitude of the combined ILM-impurity mode decreases. When the linear impurity mode frequency coincides with the driver frequency, the amplitude is now very small. If the impurity is removed suddenly as shown in Fig. 12(d), the driver cannot rapidly feed the low amplitude state so an ILM cannot be supported.

Figure 12(e) is perhaps the most interesting case shown here. An ILM is present at site 47. If we place an impurity spring constant that varies in the range (1.01–1.14)k_{2O} at the next short cantilever (site 49), the ILM is attracted to the impurity. Then, if the impurity spring constant is decreased slowly, the ILM remains at the virtual impurity location. Note the linear impurity used in this example is not strong enough to produce the "seeding" effect shown in Fig. 12(c).

The repulsive and attractive interactions in Fig. 12 are mapped as a function of the impurity linear spring constant in Figs. 13(a) and 13(b) in order to better charac-

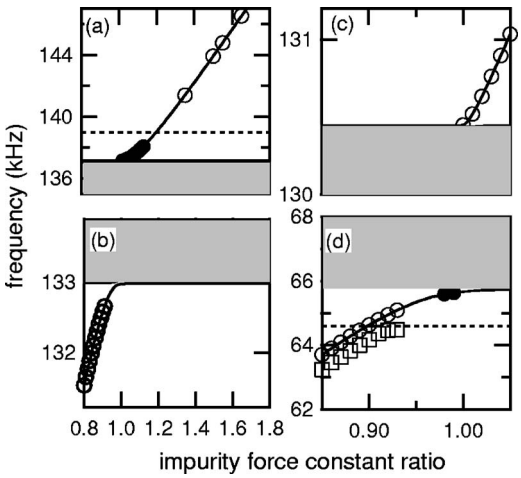

FIG. 13. Plots of the linear impurity mode frequency as a function of the impurity force constant ratio for a di-element array. (a),(b) The lattice under consideration has a hard nonlinearity. Gray area; the top and bottom of the upper opticlike band. The dotted horizontal line at 139 kHz corresponds to the cw driver frequency used in Fig. 12. Solid circles identify the linear impurity mode frequencies where an ILM attractive interaction (tweezing) is observed. Open circles identify the linear impurity mode frequencies where an ILM repulsive interaction is observed. An ILM seeding effect can be produced when the impurity force constant ratio is varied in the range from 1.14 to 1.20 with the impurity strength changed adiabatically. (c),(d) The lattice under consideration has a soft nonlinearity. Open circles and closed circles are linear impurity frequencies for the repulsive and tweezing effects, respectively. Unlike the hard nonlinear case, the repulsive interaction frequency goes between the band edge and the ILM frequency as shown in (d). Open squares, described in the text, identify the more precise nonlinear impurity mode frequencies associated with ILM repulsion.

terize the frequency relationships among the driver, the impurity mode frequency, and the opticlike cantilever band. The linear impurity mode frequencies are estimated by ignoring the nonlinear terms in Eq. (6). Impurity modes appear above and below the optic band (gray region) depending on the size of the spring constant ratio. The open circles identify impurity mode frequencies that produce ILM repulsion. Closed circles identify the attractive interaction. The driver frequency corresponds to the dotted line. In addition to the specific impurity cases described in Fig. 12, we see in Figs. 13(a) and 13(b) that with increasing impurity mode frequency there are, in general, three important ILM interaction regions: repulsion, attraction, and then repulsion again. The boundaries are the plane-wave band and the driver frequency.

The relative importance of k_{4I} and k_{4O} for the cantilever array estimated in Sec. III.A.3 is supported by these simulation results. By comparing the experimental linear impurity mode frequency produced in Fig. 7(a) with the impurity mode frequency calculation as described above, the relative spring constant change for the shorter cantilever is estimated as −10%. This is also the minimum change in the onsite spring constant required to repel an ILM in Fig. 13(b). Thus the repulsion threshold in the simulation is consistent with the experimental results. In addition we find that as long as the condition $k_{4I} > 2k_{4O}$ is satisfied (including $k_{4O}=0$), the threshold is nearly unchanged. This is not the case if $k_{4I} < 2k_{4O}$.

B. Linear impurity modes and ILMs in a soft nonlinear lattice

Experiments have shown that an ILM can be trapped by a laser-induced impurity mode in a lattice with soft nonlinearity. Here we present related simulation results for a soft nonlinear lattice induced by an electrostatic force. The equation of cantilever motion for this model is

$$m\frac{d^2x_i}{dt^2} + \frac{m}{\tau}\frac{dx_i}{dt} + k_{2Oi}x_i + k_{4Oi}x_i^3 + \sum_j k_{2I}^{(j)}(2x_i - x_{i+j} - x_{i-j}) + \sum_j k_{4I}^{(j)}[(x_i - x_{i+j})^3 + (x_i - x_{i-j})^3] + \frac{1}{2}\varepsilon_0\frac{[w(L-l)]V^2}{(d+x_i)^2} = m\alpha\cos(\Omega t), \tag{7}$$

where $k_{2Oi}=k_{2O}$ except at impurity sites, ε_0 is the permeability of free space, $S=w(L-l)$ is the surface area of the cantilever, V is the voltage, and d is the distance between the cantilever and the substrate at $V=0$. Since an ILM will occur below the driven plane-wave band, only a mono-element array need be considered. The linear spring constants are taken to be the same as those for one of the di-element lattices described earlier and are given in Table II, column 3.

Because of the two minima in the electrostatic term shown in Fig. 3(b), some care is required to find the correct parameter set for stable ILM production. When the ILM is formed, it has a much larger amplitude than the uniform mode, because the electrostatic term involves more than just the fourth-order nonlinearity. This can place the ILM in the double-valued region of the potential. We have found that the large intersite nonlinearity tends to counter this effect and stabilize ILM production. The total nonlinearity for the long-wavelength modes is soft giving rise to ILMs at the bottom of the dispersion curve; however, the large hard intersite nonlinearity changes the sign of the total nonlinearity at short wavelength and caps the ILM amplitude. Thus the condition $k_{4I} \gg k_{4O}$ found in Sec. III.A.3 is very important for maintaining vibrations in the single-valued region of the potential. Additional long-range hard nonlinear intersite spring terms have been introduced to fine-tune these stabilization results. They are assumed to have the same relative ratio as the linear spring constants,

$$\frac{k_{4I}^{(j)}}{k_{4I}^{(1)}} = \frac{k_{2I}^{(j)}}{k_{2I}^{(1)}}. \tag{8}$$

TABLE II. Micromechanical simulation parameters for three different arrays. Mass=m, relaxation time=τ, k_{2O} is the onsite harmonic spring constant, k_{2I1}–k_{2I6} are intersite harmonic spring constants for the first through sixth nearest-neighbor interactions, k_{4O} is the onsite quartic spring constant, k_{4I1}–k_{4I6} are intersite quartic spring constants for nearest up to sixth nearest-neighbor interactions, S is the cantilever surface area, d is the gap between the cantilever and the substrate, V is the dc bias voltage applied between the cantilever and the substrate, f_d is the driving frequency, and α is the acceleration of the driver. The frequencies f_1,f_2,f_3,f_4 are defined in Table I. The number in parentheses is for the shorter cantilever of the di-element array.

Type	Hard di-element lattice	Hard di-element lattice	Soft mono-element lattice
m (10^{-13} kg)	7.67 (6.98)	7.67 (6.98)	7.67
τ (ms)	8.75	8.75	8.75
k_{2O} (kg/s^2)	0.102 (0.0976)	0.142 (0.168)	0.142
k_{2I1}–k_{2I6} (kg/s^2)	0.104, 0.0405, 0.0189, 0.0118, 0.00887, 0.00346	0.0828, 0.0308, 0.0108, 0.00405, 0.00250, 0.000824	0.0828, 0.0308, 0.0108, 0.00405, 0.00250, 0.000824
k_{4O} (kg/s^2 m^2)	1.00×10^8	1.00×10^8	1.00×10^8
k_{4I1}–k_{4I6} ($\times10^{10}$ kg/s^2 m^2)	4.0, 0,0,0,0,0	4.0, 0,0,0,0,0	4.00, 1.49, 0.522, 0.195, 0.120, 0.040
S (μm^2)			55×15
d (μm)			10
V (V)			40
f_d (kHz)	147–151	139	64.6
α (m/s^2)	14000	5000	290
f_1,f_2,f_3,f_4 (kHz)	58.78, 133.3, 139.8, 147.4	73.04, 123.4, 133.0, 137.1	65.67, 130.5

The resultant ILM is rather wide, in agreement with the experiments. A distributed linear impurity mode with either a low or high frequency is constructed at 11 neighboring sites by changing the onsite spring constant ratio in the following manner:

$$\frac{k_{2Oi}}{k_{2O}} = \left(\frac{k_{2Oimp}}{k_{2O}} r_i + 1 - r_i\right), \tag{9}$$

where k_{2Oimp} is the onsite spring constant at the center of the wide impurity, r_i is the site-dependent blending factor between k_{2O} and k_{2Oimp}, which changes as $r_{i\pm5}=0.5$, $r_{i\pm4}=0.6$, …, $r_{i\pm1}=0.9$, $r_i=1.0$ thereby identifying the 11-site impurity with its center located at site i.

We start by seeding an ILM using a low-frequency impurity mode as described in Sec. VI.A. First the driver frequency is chosen to be slightly lower than the bottom of the band. From the linear eigenfrequency calculation we find that when $k_{2Oimp}=0.90k_{2O}$ the impurity resonates with the driver. The impurity strength is gradually decreased with time in the presence of the cw driver. Figure 14(a) shows that after the impurity is removed completely at $t=1500$ periods, one ILM is left. An AM modulation similar to the hard nonlinear lattice case described in Sec. VI.A can be seen.

To study the impurity interaction with this seeded ILM, the impurity is slowly moved toward the ILM in the next three examples. Figure 14(b) demonstrates the ILM repulsion produced by a high-frequency impurity mode ($k_{2Oimp}=1.10k_{2O}$). The ILM (solid) is continuously repelled by the impurity (dotted). The ILM reappears at the bottom of the figure due to the periodic boundary condition. The continuous wavy motion of the ILM indicates that the pinning effect of the ILM is weaker than for the hard nonlinear lattice case shown in Fig. 12.

Figure 14(c) shows the attractive interaction that occurs between an ILM and a low-frequency impurity mode. The impurity mode frequency is located between the bottom of the plane-wave band and the driver frequency. The ILM is attracted to the impurity even before the impurity reaches the envelope of the ILM. Similar phenomena are observed in experiment, as shown in Fig. 11, at frame 5. Once the ILM is captured, it tracks the impurity mode position. This capturing or "tweezing" of dynamical energy now permits it to be transported from site to site. Note that the impurity strength used here is not large enough to seed an ILM, as was demonstrated in Fig. 14(a). In addition, if the strength of the impurity mode is decreased, the ILM remains at that location.

Figure 14(d) shows the repulsion interaction produced by a low-frequency impurity mode located below the driver frequency. Just like the example presented in Fig. 14(b), the ILM is repelled by the impurity.

The different ILM-impurity mode interaction regions for the soft nonlinear lattice versus impurity mode frequency are mapped in Figs. 13(c) and 13(d). Unlike the hard lattice case described in Sec. VI.A, some impurity modes which appear to be located between the driver frequency and the bottom of the host band show a repulsive interaction. [See the open circles in Fig. 13(d).] A more precise calculation shows that when the nonlinear frequency shift due to a large amplitude excitation near the ILM is included, the dynamical frequencies are then renormalized below the driver frequency (open rectangles). Due to the larger widths of both the ILM and

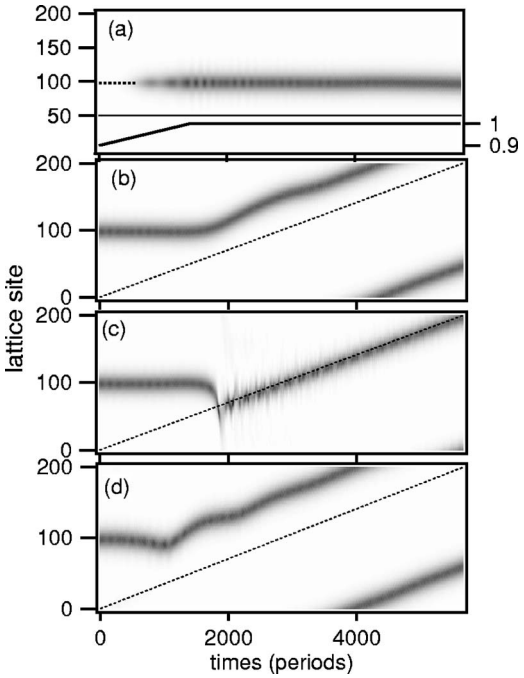

FIG. 14. Simulated time-dependent manipulation of an ILM in a soft nonlinear lattice with different impurity modes. These impurity modes are made by changing the onsite linear spring constants over 11 lattice sites, as described under Eq. (9). The central position of the 11 sites vs time is identified by the straight dotted line. (a) The seeding effect. Bottom trace: impurity force constant ratio vs time. The linear impurity frequency is resonant with the driver when the force constant ratio is 0.9. The impurity mode is fixed at site=100. (b) The repulsive interaction with the high-frequency impurity mode. The impurity force constant ratio is 1.1, and it is moved from the lower left corner to the upper right corner. The ILM is repelled. It reappears at the bottom, due to the periodic boundary condition. (c) The tweezing effect by a low-frequency impurity mode. The impurity force constant ratio is 0.99. (d) The repulsive interaction produced by a lower frequency impurity mode. The impurity force constant ratio is 0.90. Parameters are listed in Table II, column 3.

the impurity mode and the interaction-enhanced impurity mode amplitude, the nonlinear frequency shift of the impurity mode cannot be neglected. These more exact impurity mode frequencies are obtained by Fourier transforming the numerical displacements (x_i) at the impurity sites.

VII. CONCLUSIONS

A. Summary

While previous studies of individual micromechanical oscillators have focused on issues of nonlinearity and specific applications (Evoy *et al.*, 1999; Zalalutdinov *et al.*, 2000; Zalalutdinov, Olkhovets, *et al.*, 2001; Zalalutdinov, Zehnder, *et al.*, 2001; Buks and Roukes, 2002), this Colloquium has examined nonlinear-coupled arrays in order to better understand the dynamical properties of nonlinear energy localization. Using the relatively mature microelectromechanical system silicon technology, coupled cantilevers have been fabricated with individual oscillators large enough to be visualized with a CCD camera but still small enough to operate in the 100-kHz region for practical measurement times. These restrictions still permitted a range of intrinsic design parameters to examine the limits of ILM formation. The initial demonstration that ILMs could be generated in dielement micromechanical arrays was achieved by driving the lattice uniformly with a piezoelectric transducer until the large amplitude plane wave became modulationally unstable and broke up into localized excitations. With an optical lever the amplitude of vibration of a cantilever was recorded in gray scale by a one-dimensional CCD camera. Although it is not possible to distinguish between a cantilever in the up and down positions, this optical method permitted the visualization of the dynamical envelope of an ILM. Chirping the frequency of the driver provided an efficient means of injecting energy into the system, and sometimes created spatially pinned ILMs that were frequency locked to the driver. Other phenomena observed included a repulsive interaction between a stable locked ILM and a moving unlocked ILM, and site-to-site hopping of locked ILMs.

Localized energy manipulation and the demonstration of targeted energy transfer are important experimental observations. In the continuously driven state a central feature is localized energy manipulation via the repulsive or attractive interaction between a focused laser beam and an ILM in a hard or soft nonlinear cantilever array. The local heating by the laser optically induces a real time impurity mode that can be used to create, destroy, repel, or attract an ILM depending on the sign of the nonlinearity in the lattice.

B. Other systems and future prospects

The localization of energy observed for nonlinear periodic cantilevers should be relevant to modern engineering problems. The vibration-induced fatigue failure of jet engine rotor blades is such a case. This complex problem can be traced back to the observed fluttering of bladed disks as a function of revolution speed, a fundamental vibrational problem that has been studied intensely for 35 years (Srinivasan, 1997). The large and localized vibrational blade amplitudes under forced response that are observed to appear at some speeds are not predicted for a tuned linear system. These observations have been described repeatedly in terms of variations in blade geometry and/or blade homogeneity and the task of controlling and predicting the vibrational amplitudes of mistuned bladed disks remains an active research area (Sever, 2004). From this Colloquium it is clear that even a bladed disk containing homogeneous blades of exactly the same geometry and composition can, given the right conditions, undergo a modulational instability at certain rotational speeds and produce large amplitude localized vibrations simply because each perfect nonlinear blade is coupled to its neighbors.

Whether or not ILMs can occur in condensed-matter crystals in equilibrium is still under discussion. Near many paraelectric to ferroelectric phase transitions the temperature dependence of the transverse optic mode is produced by the near cancellation of the harmonic short-range and long-range forces (Cochran, 1959), so that crystal anharmonicity becomes increasingly important. Such phase-transition temperature regions may provide a natural habitat for dynamical energy localization. The appearance of spatially localized intrinsic resonant modes with their associated diffusive translational motion could account for the unusual dynamic and static properties observed just above the transition (Hayes and Loudon, 1978; Lyons and Fleury, 1978; Luspin *et al.*, 1980; Fleury and Lyons 1983; Sokoloff *et al.*, 1988).

Particularly noteworthy in this Colloquium has been the use of optical tweezers to trap and manipulate localized dynamical energy, instead of particles. This impurity mode production method should be applicable to any nonlinear discrete lattice, even those at the atomic scale. By introducing an appropriate external movable probe, control methods may be developed for identifying and counting nanoscale ILMs. One such probe could be a scanning force microscope tip at the surface of an atomic lattice.

ACKNOWLEDGMENTS

We thank A. R. Bishop, H. G. Craighead, S. Flach, B. Ilic, P. G. Kevrekidis, J. B. Page, J. Parpia, S. Takeno, and J. P. Wrubel for helpful comments. This material is based upon work supported by the National Science Foundation under Grant No. 0301035, the Department of Energy under Grant No. DE-FG02-04ER46154, the National Research Council Twinning Program, and the Cornell Center for Materials Research. The samples were prepared at the Cornell Nanofabrication Facility, which is also supported by the NSF.

APPENDIX: FROM ELASTIC CONTINUUM TO A DISCRETE LATTICE MODEL

1. Derivation of the lumped element single cantilever equation of motion

The Euler-Bernoulli beam theory (Crespo da Silva and Glynn, 1978; Malatkar and Nayfeh, 2003) provides a continuum equation of motion describing a single cantilever. The resulting expression for the case of hard nonlinearity is

$$\rho A\frac{\partial^2 u}{\partial t^2}+EI\frac{\partial^4 u}{\partial s^4}+EI\frac{\partial}{\partial s}\left[\frac{\partial u}{\partial s}\frac{\partial}{\partial s}\left(\frac{\partial u}{\partial s}\frac{\partial^2 u}{\partial s^2}\right)\right]=\rho A\alpha\cos(\Omega t), \tag{A1}$$

where ρ is the cantilever density, A is the cross-sectional area of the cantilever beam, E is Young's modulus of the material, $I=1/(12wh^3)$ is the second moment of inertia (also called the moment of area) (Landau and Lifshitz, 1970) where w is the width and h is the thickness of the beam, α is the acceleration amplitude, and Ω is the external driving frequency. The beam displacement $u(s,t)$ is a function of the continuous arc coordinate s (measured along the length of the cantilever from the fixed end) and the time. The first two terms of Eq. (A1) describe the linearized (small amplitude motion) portion that will typically appear in a textbook on the subject of beam vibration (Timoshenko *et al.*, 1974; Cleland, 2003). The third term identifies the nonlinear restoring force that results from large beam deflections and is often referred to as the geometric nonlinearity (Crespo da Silva and Glynn, 1978; Malatkar, 2003).

To make contact with Eq. (1) only the time-dependent dynamics of the tip of the cantilever beam ($s=L$) is of interest. A procedure for eliminating the variable s is now outlined (Crespo da Silva and Glynn, 1978; Malatkar and Nayfeh, 2003). The linear part of Eq. (A1) (first and second terms) provides an orthonormal set of shape functions, where the nth normal mode is $\varphi_n(s)$ with frequency ω_n. The variable $u(s,t)$ is then expanded in terms of this set so that, in general,

$$u(s,t)=\sum_n \varphi_n(s)\chi_n(t). \tag{A2}$$

In our case only the lowest frequency mode is of interest so that $u(s,t)=\varphi_1(s)\chi_1(t)$, where $\chi_1(t)$ has the dimension of length (displacement). Taking the inner product of $\varphi_1(s)$ with Eq. (A1) and numerically evaluating the resulting integrals gives

$$m\frac{d^2}{dt^2}\chi(t)+\frac{12.36EI}{L^3}\chi(t)+\frac{40.44EI}{L^5}\chi^3(t)=0.783m\alpha\cos(\Omega t), \tag{A3}$$

where $m=\rho AL$ is the cantilever mass. This expression has the form of a Duffing equation (Cleland, 2003). Since $\varphi_1=2$ at the tip of the cantilever, $\chi(t)$ is one-half of the tip amplitude. Introducing a new variable $x(t)=2\chi(t)$ for the tip amplitude, Eq. (A3) becomes Eq. (2) in the text, namely,

$$m\frac{d^2}{dt^2}x(t)+\frac{12.36EI}{L^3}x(t)+\frac{10.11EI}{L^5}x^3(t)=1.566m\alpha\cos(\Omega t), \tag{2}$$

and the hard quartic spring constant for the mass and spring model is $k_4=10.11EI/L^5$.

2. Estimate of the hard *intersite* nonlinearity for the lumped element model

We are particularly interested in examining the expression for the lowest frequency mode at the center of the overhang, which is the location of the actual cantilever. The equation of motion at this location is

$$hp\rho\frac{d^2}{dt^2}u(s,t)+\frac{h^3E}{12}\frac{\pi^4}{p^3}u(s,t)+\frac{hE}{4}\frac{\pi^4}{p^3}u^3(s,t)=0, \quad \text{(A4)}$$

where s measures the distance from the fixed boundary along the actual cantilever direction, as in the previous section, p is the lattice constant (pitch) of the array [see the inset in Fig. 3(c)], and $u(s,t)$ is the deformation at the middle of the bar element. (For the zone-boundary mode of the mono-element-type array the acceleration driving force is omitted.) The third term describes the hard nonlinear force acting at the point s. We now describe the overhang region involving one cantilever of the array as a series of neighboring minibars with the midpoint of each one having a deformation amplitude which varies with s. To evaluate the nonlinear force acting on the tip of the cantilever, Eq. (A4) is handled the same way as was Eq. (A1): the amplitude is written as $u(s,t)=\varphi_1(s)\chi(t)$ and then the inner product of $\varphi_1(s)$ with Eq. (A4) is evaluated to give

$$0.102m_{\text{over}}\frac{d^2}{dt^2}\chi(t)+0.004\,23\frac{\pi^4h^3EL}{p^3}\chi(t)+0.003\,32\frac{hE\pi^4L}{p^3}\chi^3(t)=0, \quad \text{(A5)}$$

where $m_{\text{over}}=\rho hpl$ is the overhang mass. Here the cantilever coordinate is integrated from $s=0$ to the overhang limit $s=l$, defined in the inset in Fig. 3(c). A typical ratio in these fabricated systems is that $l\approx L/2$ so this value is used in our estimate. Again using $x(t)=2\chi(t)$ for the tip amplitude in Eq. (A5) gives Eq. (4) in the text, i.e.,

$$0.102m_{\text{over}}\frac{d^2}{dt^2}x(t)+0.004\,23\frac{\pi^4h^3EL}{p^3}x(t)+0.000\,831\frac{hE\pi^4L}{p^3}x^3(t)=0. \quad \text{(4)}$$

REFERENCES

Aksyuk, V. A., S. Arney, N. R. Basavanhally, D. J. Bishop, C. A. Bolle, C. C. Chang, R. Frahm, A. Gasparyan, J. V. Gates, R. George, C. Giles, J. Kim, P. Kolodner, T. Lee, D. Neilson, C. Nijander, C. Nuzman, A. Paczkowski, A. Papazian, F. Pardo, D. Ramsey, R. Ryf, R. Scotti, H. Shea, and M. Simon, 2003, IEEE Photonics Technol. Lett. **15**, 587.

Austin, R. H., A. H. Xie, L. van der Meer, M. Shinn, and G. Neil, 2003, J. Phys.: Condens. Matter **15**, S1693.

Bang, O., and P. D. Miller, 1996, Opt. Lett. **21**, 1105.

Bang, O., and M. Peyrard, 1995, Physica D **81**, 9.

Barker, A. S., and A. J. Sievers, 1975, Rev. Mod. Phys. **47**, S1.

Bickham, S. R., S. A. Kiselev, and A. J. Sievers, 1997, in *Spectroscopy and Dynamics of Collective Excitations in Solids*, edited by B. Di Bartolo (Plenum, New York), p. 247.

Bickham, S. R., A. J. Sievers, and S. Takeno, 1992, Phys. Rev. B **45**, 10344.

Bickham, S. R., A. J. Sievers, and S. Takeno, 1993, in *Defects in Insulating Materials*, edited by O. Kanert and J.-M. Spaeth (World Scientific, Schloss Nordkirchen, Germany), p. 531.

Bilz, H., D. Strauch, and R. K. Wehner, 1984, *Vibrational Infrared and Raman Spectra of Non-Metals* (Springer-Verlag, Berlin).

Binder, P., D. Abraimov, A. V. Ustinov, S. Flach, and Y. Zolotaryuk, 2000, Phys. Rev. Lett. **84**, 745.

Bishop, D. J., C. R. Giles, and S. R. Das, 2001, Sci. Am. (Int. Ed.) **284**, 88.

Bourbonnais, R., and R. Maynard, 1990, Phys. Rev. Lett. **64**, 1397.

Bourbonnais, R., and R. Maynard, 1992, Int. J. Mod. Phys. C **1**, 233.

Brillouin, L., 1946, *Wave Propagation in Periodic Structures* (McGraw Hill, New York).

Buks, E., and M. L. Roukes, 2002, J. Microelectromech. Syst. **11**, 802.

Burlakov, V. M., and S. A. Kiselev, 1991, Sov. Phys. JETP **72**, 854.

Buser, R. A., and N. F. de Rooij, 1989, Sens. Actuators **17**, 145.

Cai, D., A. R. Bishop, and N. Gronbech-Jensen, 1994, Phys. Rev. Lett. **72**, 591.

Campbell, D. K., S. Flach, and Y. S. Kivshar, 2004, Phys. Today **57** (1), 43.

Chan, H. B., V. A. Aksyuk, R. N. Kleiman, D. J. Bishop, and F. Capasso, 2001, Phys. Rev. Lett. **87**, 211801.

Chen, W., 1994, Phys. Rev. B **49**, 15063.

Christoldoulides, D. N., and R. I. Joseph, 1988, Opt. Lett. **13**, 794.

Cleland, A. N., 2003, *Foundations of Nanomechanics: From Solid-State Theory to Device Applications* (Springer, Berlin), p. 314.

Cochran, W., 1959, Phys. Rev. Lett. **3**, 412.

Crespo da Silva, M. R. M., and C. C. Glynn, 1978, J. Struct. Mech. **6**, 449.

Daumont, I., T. Dauxois, and M. Peyrard, 1997, Nonlinearity **10**, 1.

Dauxois, T., and M. Peyrard, 1993, Phys. Rev. Lett. **70**, 3935.

Debye, P., 1912, Ann. Phys. **39**, 789.

Dolgov, A. S., 1986, Sov. Phys. Solid State **28**, 907.

Edler, J., and P. Hamm, 2004, Phys. Rev. B **69**, 214301.

Eisenberg, H. S., Y. Silberberg, R. Morandotti, A. R. Boyd, and J. S. Aitchson, 1998, Phys. Rev. Lett. **81**, 3383.

English, L. Q., M. Sato, and A. J. Sievers, 2001, J. Appl. Phys. **89**, 6707.

Evoy, S., D. W. Carr, L. Sekaric, A. Olkhovets, J. M. Parpia, and H. G. Craighead, 1999, J. Appl. Phys. **86**, 6072.

Fauver, M. E., D. L. Dunaway, D. H. Lilienfeld, and H. G. Craighead, 1998, IEEE Trans. Biomed. Eng. **45**, 891.

Fehske, H., M. Kinateder, G. Wellein, and A. R. Bishop, 2001, Phys. Rev. B **63**, 245121.

Fehske, H., G. Wellein, H. Buttner, A. R. Bishop, and M. I. Salkola, 2000, Physica B **281**, 673.

Fermi, E., J. R. Pasta, and S. M. Ulam, 1955, *Collected Works of E. Fermi* (University of Chicago Press, Chicago),

Flach, S., 2004, in *Energy Localisation and Transfer*, edited by T. Dauxois, A. Litvak-Hinenzon, R. MacKay, and A. Spanoudaki (World Scientific, London), p. 1.

Flach, S., and C. R. Willis, 1994, Phys. Rev. Lett. **72**, 1777.

Flach, S., and C. R. Willis, 1998, Phys. Rep. **295**, 182.
Flach, S., C. R. Willis, and E. Olbrich, 1993, Phys. Rev. E **49**, 836.
Fleischer, J. W., T. Carmon, M. Segev, N. K. Efremidis, and D. N. Christodoulides, 2003, Phys. Rev. Lett. **90**, 023902.
Fleischer, J. W., M. Segev, N. K. Efremidis, and D. N. Christodoulides, 2003, Nature (London) **422**, 147.
Fleury, P. A., and K. B. Lyons, 1983, in *Light Scattering near Phase Transitions*, edited by H. Z. Cummins and A. P. Levanyuk (North-Holland, Amsterdam), p. 449.
Grant, A. R., A. J. Sievers, J. H. Harding, and M. J. L. Sangster, 1998, Phys. Rev. Lett. **81**, 3687.
Greene, L. H., and A. J. Sievers, 1982, Solid State Commun. **44**, 1325.
Hayes, W., and R. Loudon, 1978, *Scattering of Light by Crystals* (Wiley, New York).
Ilic, B., D. Czaplewski, H. G. Craighead, P. Neuzil, C. Campagnolo, and C. Batt, 2000, Appl. Phys. Lett. **77**, 450.
Kevrekidis, P. G., and B. A. Malomed, 2002, Phys. Lett. A **303**, 328.
Kiselev, S. A., S. R. Bickham, and A. J. Sievers, 1993, Phys. Rev. B **48**, 13508.
Kiselev, S. A., S. R. Bickham, and A. J. Sievers, 1994, Phys. Rev. B **50**, 9135.
Kiselev, S. A., S. R. Bickham, and A. J. Sievers, 1995, Comments Condens. Matter Phys. **17**, 135.
Kiselev, S. A., and A. J. Sievers, 1997, Phys. Rev. B **55**, 5755.
Kivshar, Y. S., 1991, Phys. Lett. A **161**, 80.
Kivshar, Y. S., and D. K. Campbell, 1993, Phys. Rev. E **48**, 3077.
Kivshar, Y. S., and M. Peyrard, 1992, Phys. Rev. A **46**, 3198.
Kosevich, A. M., 2003, private communication.
Lai, R., and A. J. Sievers, 1999, Phys. Rep. **314**, 147.
Landau, L. D., and E. M. Lifshitz, 1970, *Theory of Elasticity* (Pergamon, Oxford).
Lifshitz, R., and M. C. Cross, 2003, Phys. Rev. B **67**, 134302.
Lou, S., and G. Huang, 1995, Mod. Phys. Lett. B **9**, 1231.
Luspin, Y., J. L. Servoin, and F. Gervais, 1980, J. Phys. C **13**, 3761.
Lyons, K. B., and P. A. Fleury, 1978, Phys. Rev. B **17**, 2403.
Malatkar, P., 2003, Ph.D. thesis (Virginia Polytechnic Institute, Blacksburg).
Malatkar, P., and A. H. Nayfeh, 2003, Nonlinear Dyn. **31**, 225.
Mandelik, D., H. S. Eisenberg, Y. Silberberg, R. Morandotti, and J. S. Aitchison, 2003, Phys. Rev. Lett. **90**, 253902.
Maradudin, A. A., 1969, in *Elementary Excitations in Solids*, edited by A. A. Maradudin and G. F. Nardelli (Plenum, New York), p. 35.
Maradudin, A. A., E. W. Montroll, G. H. Weiss, and I. P. Ipatova, 1971, *Theory of Lattice Dynamics in the Harmonic Approximation* (Academic, New York).
Marion, J. B., 1970, *Classical Dynamics of Particles and Systems*, 2nd ed. (Academic, New York), p. 153.
Markovich, T., E. Polturak, J. Bossy, and E. Farhi, 2002, Phys. Rev. Lett. **88**, 195301.
Marquie, P., J. M. Bilbault, and M. Remoissenet, 1995, Phys. Rev. E **51**, 6127.
McGurn, A. R., 2002, Phys. Rev. B **65**, 1.
Mohanty, P., D. A. Harrington, K. L. Ekinci, Y. T. Yang, M. J. Murphy, and M. L. Roukes, 2004, Phys. Rev. B **66**, 085416.
Newman, R. C., 1969, Adv. Phys. **18**, 545.
Page, J. B., 1990, Phys. Rev. B **41**, 7835.
Press, W. H., S. A. Teukosky, W. T. Vetterling, and B. P. Flannery, 1992, *Numerical Recipes in Fortran 77* (Cambridge University Press, Cambridge, England).
Rakhmanova, S., and D. L. Mills, 1996, Phys. Rev. B **54**, 9225.
Remoissenet, M., 1999, *Waves Called Solitons* (Springer-Verlag, Berlin).
Rössler, T., and J. B. Page, 1995, Phys. Lett. A **204**, 418.
Rössler, T., and J. B. Page, 1997, Phys. Rev. Lett. **78**, 1287.
Rössler, T., and J. B. Page, 2000, Phys. Rev. B **62**, 11460.
Rouxel, T., J.-C. Sangleboeuf, M. Huger, C. Gault, J.-L. Besson, and S. Testu, 2002, Acta Mater. **50**, 1669.
Sandusky, K. W., and J. B. Page, 1994, Phys. Rev. B **50**, 866.
Sandusky, K. W., J. B. Page, and K. E. Schmidt, 1992, Phys. Rev. B **46**, 6161.
Sandusky, K. W., A. Rosenberg, C. E. Mungan, and A. J. Sievers, 1991, Phys. Rev. Lett. **67**, 871.
Sato, M., L. Q. English, B. E. Hubbard, and A. J. Sievers, 2002, J. Appl. Phys. **91**, 8676.
Sato, M., B. E. Hubbard, L. Q. English, A. J. Sievers, B. Ilic, D. A. Czaplewski, and H. G. Craighead, 2003, Chaos **13**, 702.
Sato, M., B. E. Hubbard, A. J. Sievers, B. Ilic, and H. G. Craighead, 2004, Europhys. Lett. **66**, 318.
Sato, M., B. E. Hubbard, A. J. Sievers, B. Ilic, D. A. Czaplewski, and H. G. Craighead, 2003, Phys. Rev. Lett. **90**, 044102.
Sato, M., and A. J. Sievers, 2004, Nature (London) **432**, 486.
Schwarz, U. T., L. Q. English, and A. J. Sievers, 1999, Phys. Rev. Lett. **83**, 223.
Sekaric, L., D. W. Carr, S. Envoy, J. M. Parpia, and H. G. Craighead, 2002, Sens. Actuators, A **101**, 215.
Sekaric, L., J. M. Parpia, H. G. Craighead, T. Feygelson, B. H. Houston, and J. E. Butler, 2004, Appl. Phys. Lett. **81**, 4455.
Sever, I. A., 2004, Ph.D. thesis (Imperial College, London).
Sievers, A. J., 1969, in *Elementary Excitations in Solids*, edited by A. A. Maradudin and G. F. Nardelli (Plenum, New York), p. 193.
Sievers, A. J., and J. B. Page, 1995, in *Dynamical Properties of Solids: Phonon Physics The Cutting Edge*, edited by G. K. Horton and A. A. Maradudin (North-Holland, Amsterdam), p. 137.
Sievers, A. J., and S. Takeno, 1988, Phys. Rev. Lett. **61**, 970.
Sokoloff, J. P., L. I. Chase, and D. Rytz, 1988, Phys. Rev. B **38**, 597.
Srinivasan, A. V., 1997, J. Eng. Gas Turbines Power **119**, 742.
Swanson, B. I., J. A. Brozik, S. P. Love, G. F. Strouse, A. P. Shreve, A. R. Bishop, W.-Z. Wang, and M. I. Salkola, 1999, Phys. Rev. Lett. **82**, 3288.
Timoshenko, S., D. H. Young, and J. W. Weaver, 1974, *Vibration Problems in Engineering* (Wiley, New York).
Toda, M., 1989, *Theory of Nonlinear Lattices*, 2nd ed., Springer Series in Solid-State Sciences (Springer-Verlag, Berlin), p. 23.
Trías, E., J. J. Mazo, and T. P. Orlando, 2000, Phys. Rev. Lett. **84**, 741.
Ustinov, A. V., 2003, Chaos **13**, 716.
Wallis, R. F., D. L. Mills, and A. D. Boardman, 1995, Phys. Rev. B **52**, R3828.
Wang, W. Z., A. R. Bishop, J. T. Gammel, and R. N. Silver, 1998, Phys. Rev. Lett. **80**, 3284.
Woinowsky-Krieger, S., 1950, Trans. ASME, J. Appl. Mech. **17**, 35.
Xie, A., L. van der Meer, W. Hoff, and R. H. Austin, 2000, Phys. Rev. Lett. **84**, 5435.
Younis, M. I., and A. H. Nayfeh, 2003, Nonlinear Dyn. **31**, 91.
Zabusky, N., and M. Kruskal, 1965, Phys. Rev. Lett. **15**, 240.

Zalalutdinov, M., B. Ilic, D. Czaplewski, A. Zehnder, H. G. Craighead, and J. M. Parpia, 2000, Appl. Phys. Lett. **77**, 3287.
Zalalutdinov, M., A. Olkhovets, A. Zehnder, B. Ilic, D. Czaplewski, H. G. Craighead, and J. M. Parpia, 2001, Appl. Phys. Lett. **78**, 3142.
Zalalutdinov, M., A. Zehnder, A. Olkhovets, S. Turner, L. Sekaric, B. Ilic, D. Czaplewski, J. M. Parpia, and H. G. Craighead, 2001, Appl. Phys. Lett. **79**, 695.
Zheng, Z. G., M. C. Cross, and G. Hu, 2002, Phys. Rev. Lett. **89**, 154102.